remote sensing

MDPI

Article

Four Years of Atmospheric Boundary Layer Height Retrievals Using COSMIC-2 Satellite Data

Ginés Garnés-Morales [1,2], Maria João Costa [3,4], Juan Antonio Bravo-Aranda [1,5], María José Granados-Muñoz [1,5], Vanda Salgueiro [3,4], Jesús Abril-Gago [1,5], Sol Fernández-Carvelo [1,5], Juana Andújar-Maqueda [1,5], Antonio Valenzuela [1,5], Inmaculada Foyo-Moreno [1,5], Francisco Navas-Guzmán [1,5], Lucas Alados-Arboledas [1,5], Daniele Bortoli [3,4] and Juan Luis Guerrero-Rascado [1,5,*]

1 Andalusian Institute for Earth System Research (IISTA-CEAMA), 18006 Granada, Spain; ginesgm@correo.ugr.es (G.G.-M.); jabravo@ugr.es (J.A.B.-A.); mjgranados@ugr.es (M.J.G.-M.); jabrilgago@ugr.es (J.A.-G.); solfcarvelo@ugr.es (S.F.-C.); juaniandujar@ugr.es (J.A.-M.); avalenzuela@ugr.es (A.V.); ifoyo@ugr.es (I.F.-M.); fguzman@ugr.es (F.N.-G.); alados@ugr.es (L.A.-A.)
2 Regional Atmospheric Modeling Lab (G-MAR), Department of Physics, Regional Campus of International Excellent 'Campus Mare Nostrum' (CEIR), University of Murcia, 30100 Murcia, Spain
3 Institute of Earth Sciences (ICT) and Earth Remote Sensing Laboratory (EaRSLab), 7000-671 Évora, Portugal; mjcosta@uevora.pt (M.J.C.); vsalgueiro@uevora.pt (V.S.); db@uevora.pt (D.B.)
4 Department of Physics, University of Évora, 7000-671 Évora, Portugal
5 Department of Applied Physics, University of Granada, 18071 Granada, Spain
* Correspondence: rascado@ugr.es

Abstract: This work aimed to study the atmospheric boundary layer height (ABLH) from COSMIC-2 refractivity data, endeavoring to refine existing ABLH detection algorithms and scrutinize the resulting spatial and seasonal distributions. Through validation analyses involving different ground-based methodologies (involving data from lidar, ceilometer, microwave radiometers, and radiosondes), the optimal ABLH determination relied on identifying the lowest refractivity gradient negative peak with a magnitude at least τ% times the minimum refractivity gradient magnitude, where τ is a fitting parameter representing the minimum peak strength relative to the absolute minimum refractivity gradient. Different τ values were derived accounting for the moment of the day (daytime, nighttime, or sunrise/sunset) and the underlying surface (land or sea). Results show discernible relations between ABLH and various features, notably, the land cover and latitude. On average, ABLH is higher over oceans (≈1.5 km), but extreme values (maximums $>$ 2.5 km, and minimums $<$ 1 km) are reached over intertropical lands. Variability is generally subtle over oceans, whereas seasonality and daily evolution are pronounced over continents, with higher ABLHs during daytime and local wintertime (summertime) in intertropical (middle) latitudes.

Keywords: boundary layer; COSMIC-2; refractivity profile; satellite calibration

Citation: Garnés-Morales, G.; Costa, M.J.; Bravo-Aranda, J.A.; Granados-Muñoz, M.J.; Salgueiro, V.; Abril-Gago, J.; Fernández-Carvelo, S.; Andújar-Maqueda, J.; Valenzuela, A.; Foyo-Moreno, I.; et al. Four Years of Atmospheric Boundary Layer Height Retrievals Using COSMIC-2 Satellite Data. *Remote Sens.* **2024**, *16*, 1632. https://doi.org/10.3390/rs16091632

Academic Editor: Mark Bourassa

Received: 19 March 2024
Revised: 22 April 2024
Accepted: 29 April 2024
Published: 3 May 2024

1. Introduction

The atmospheric boundary layer (ABL), also known as the planetary boundary layer (PBL), is the lowest layer of the troposphere. The ABL is directly influenced by the Earth's surface, with which it continuously interacts [1], and responds to its direct forcings on time scales of one hour or less, while indirect effects (e.g., in the residual layer, RL) can extend to daily time scales. These forcings encompass frictional drag, evapotranspiration, heat transfer, pollutant emissions, and terrain-induced flux modification [2].

The thickness of the ABL varies in time and space. Over land, in situations popularly characterized as fair weather, the ABL exhibits a well-marked daily cycle [3]. During daytime, a highly turbulent mixed layer (CBL, convective boundary layer) grows in height, and above this, the entrainment zone is located, a statically stable layer of intermittent turbulence. As sunset approaches, turbulence decays, leaving an RL previously occupied

the CBL. During nighttime, the bottom of the ABL turns into a stable boundary layer (SBL) due to contact with the Earth's surface, cooled by the emission of longwave radiation. Over oceans, however, the daily cycle of the ABL is usually rather indistinguishable because of a persistent capping inversion [4–6]. Convective conditions predominate in oceanic regions with unstable stratification even during nighttime, so the RL is more infrequent [7]. It should be pointed out that there is some controversy among authors about whether or not the RL belongs to the ABL. For instance, Stull [2] does not include the RL as an ABL layer, but the American Meteorological Society, in its glossary, defines the RL as a part of the ABL (https://glossary.ametsoc.org/wiki/Residual_layer, last accessed on 12 February 2024). In this work, the RL is considered to belong to the ABL. The ABL height (ABLH), i.e., the top of the ABL, is the height above the surface where the influence of the Earth's surface becomes weak and the transition to the free troposphere (FT) begins.

The ABL defines the volume in which gases and aerosols originating from the Earth's surface are mainly dispersed. It plays a crucial role in the exchange of momentum, heat, moisture, and particles, as well as greenhouse gases, between the surface and the atmosphere [2,8,9]. Ultimately, the importance of ABL lies in the fact that its processes directly affect society since life develops within the ABL, and indirectly through its influence on meteorology [10]. This is the reason why a deep understanding of the ABL dynamics would lead to a positive impact on a large number of applications in the social, economic, and health fields, including air quality assessment [11], renewable energy generation [12], numerical weather prediction [13], sustainable urban planning [14], and all types of aspects related to transport including aviation, navigation, and road safety [15]. However, despite its relevance, quantitative knowledge of ABL concerning its temporal and spatial variations is still limited due to the complexity of the techniques involved, instrumental limitations, and the lack of consensus in the scientific community on concepts involved in boundary layer studies.

Traditionally, ABL monitoring has been achieved utilizing radiosondes. While these provide very useful information, their temporal resolution is typically insufficient to capture the complete daily evolution of ABL dynamics [16]. In addition, the horizontal drift of sounding balloons causes observations to be affected by spatial variations in ABL dynamics that might be difficult to analyze and interpret.

Over recent decades, progress in ground-based remote sensing techniques has allowed for narrowing this gap, providing high-resolution information, initially focused on the first kilometer of the atmosphere (see revisions of Wilczak et al. [17] and Emeis et al. [18]). Significant advances in this technology and the development of computational algorithms make it possible nowadays to profile the full extent of the ABL (covering from the first tens of meters to more than 3 km in height, and even more if the geographical and synoptic conditions are adequate) with high temporal and vertical resolution [13,19], and detect ABLH, as well as the height of ABL sublayers, from different atmospheric properties [10,20,21].

Besides techniques based on surface instruments, some sensors on board satellites can also be used to extract information about the ABL. Among these are the aerosol lidar aboard CALIPSO (Cloud-Aerosol Lidar and Infrared Pathfinder Satellite Observations) [22,23] and the ALADIN (Atmospheric Laser Doppler Instrument) Doppler wind lidar on board Aeolus [24–27]. Satellite observations tend to be less suitable for studying shallow layers (e.g., Aeolus-ALADIN is not adequate to monitor the conditions of superficial layers [26]) or for detecting the height of ABL sublayers owing to the degradation of profiles near the surface [28,29] and the relatively low horizontal resolution (87 km approximately for Aeolus), which introduces additional errors, especially in coastal zones and complex topography [30]. Even so, ABLHs retrieved from satellite observations are highly valuable, as these data constitute consistent measurements on a global scale [31] whose seasonal cycle is an important constraint on the behavior of global atmospheric models [6,32].

A promising technique that also involves space technology is radio occultation (RO). Particularly, GNSS-RO (Global Navigation Satellite System Radio Occultation; refs. [6,29,30,33,34]) is a remote sensing technique that makes use of GNSS signals (e.g., GPS)

received by low Earth orbit (LEO) satellites to profile the Earth's atmosphere and ionosphere with high vertical resolution and global coverage. This, along with its high precision, makes GNSS-RO data very appropriate for a wide range of studies on weather forecasting, atmospheric processes, climate monitoring, model validation, space weather, and the ionosphere, among others.

The science behind RO was first developed in the 1960s [35,36] to analyze the atmospheres of planets outside the solar system. During the 1990s, scientists began to apply this technique to study the Earth's atmosphere [37–39]. The method is based on the fact that radio signals emitted by GNSS satellites (already in orbit) get refracted and slowed down as they pass through the atmosphere owing to interactions with molecules and electrons. LEO satellites intercept the disturbed signal and measure its bending angle and delay. Then, inversion algorithms are applied to retrieve vertical profiles of meteorological variables such as refractivity, temperature, pressure, humidity, and electron density.

The COSMIC (Constellation Observing System for Meteorology, Ionosphere and Climate) Program, driven by UCAR (the University Corporation for Atmospheric Research), has been one of the leaders in the collection and scientific application of GNSS data since UCAR itself demonstrated the potential of using RO to probe the Earth's atmosphere in the GPS/MET experiment between 1995 and 1997 [38,40]. It contributed to the design, management, and operation of the FORMOSAT-3/COSMIC-1 (COSMIC-1) mission from 2006 to 2020 [40]. This mission has provided high-quality RO profiles with significant positive impact in the fields of meteorology research and space weather [41–43]. Given the success of the COSMIC-1 mission, the organizations involved, including several US agencies (led by the National Oceanic and Atmospheric Administration (NOAA)) and Taiwanese agencies (primarily the National Space Organization (NSPO)), planned a second mission named FORMOSAT-7/COSMIC-2 (COSMIC-2). Consequently, on 25 June 2019, six new satellites incorporating the next generation of GNSS-RO technology were launched in low-inclination orbits. Since 1 October 2019, the COSMIC-2 mission has provided more than 4000 profiles per day with great resolution and deep penetration into the troposphere (50% of profiles reach 200 m above the surface). This offers a revolutionary increase in the number of atmosphere and ionosphere observations, as well as an extraordinary database for the scientific community. Moreover, various works note that COSMIC-2 data enhance the detection of ABLH and super-refraction at the ABL top [43,44].

There is no device capable of measuring ABLH directly. Instead, properties of some variables, such as refractivity, temperature, humidity, wind, or aerosol backscatter coefficient, are considered to estimate the ABLH. The recent work of Kotthaus et al. [10] summarizes the state-of-the-art techniques to locally profile the ABL and the diverse methods to retrieve its height, pointing out both their abilities and limitations. Depending on the available experimental device used, its built-in sensors, the variables they measure, and the meteorological and geographical conditions, one methodology might be more convenient than another. Furthermore, quantifying the uncertainty of the results is not simple, as there is no universal method that can provide an unequivocal value that can be used as an absolute reference [10]. In fact, besides the physical background behind the upper limit of the ABL, many proposed algorithms, such as those presented in Liu and Liang [7] and Santosh [45], are based on the empirical experience in order to reduce the practical complexity of the ABLH retrievals and to develop methodologies that maximize agreement with the most reliable observations (normally radiosoundings). Currently, studies that use GNSS-RO data to estimate the ABLH often rely on bending angle or refractivity profiles. Qiu et al. [46] assessed the reliability and accuracy of several methods to calculate the ABLH by using bending angle and refractivity data from COSMIC-2 and Spire missions. They concluded that the minimum bending angle gradient method [47] was the most suitable, as it provided the highest correlations and minimum bias with respect to their chosen reference method (minimum gradient of temperature and relative humidity, whose data came from radiosondes). Likewise, the minimum refractivity gradient [30,34] and breaking point [48] methods showed promising performance. Santosh [45] carried out a

global-scale seasonal study of daytime ABLH utilizing the first two years of COSMIC-2 refractivity data, in which they proposed a new algorithm for ABLH estimation derived from the minimum refractivity gradient method, a modification endorsed by a validation analysis with radiosounding data.

This work aims to perform a study of the ABLH using the first four years of refractivity data from the COSMIC-2 mission. With this purpose, an attempt is made to improve and extend the ABLH estimation algorithm proposed by Santosh [45], which only considers diurnal instability cases, and is exclusively validated with data from radiosondes launched at standard times. In this work, the goodness of the algorithm is assessed by comparing with results obtained through other methodologies, which involve different instruments and variables continuously monitored throughout the day, as well as radiosounding data. Specifically, the objectives of this contribution are (i) to propose an enhanced algorithm to detect ABLH from refractivity profiles, considering the intradiurnal variability and distinguishing, in a certain way, land and oceanic areas, and (ii) to scrutinize the spatial and seasonal distribution of ABLH resulting from the proposed algorithm.

In Section 2, the characteristics of the instruments, data and the methods employed are described. The results are addressed in Section 3. Section 4 is devoted to the discussion. Finally, the conclusions of the study are presented in Section 5.

2. Materials and Methods

2.1. Instrumentation and Databases

In this study, we make use of measurements from the microwave radiometer (MWR) and the ceilometer installed at the Andalusian Institute for Earth System Research (IISTA-CEAMA) in Granada (Spain) (37.164°N, 3.605°W, 680 m a.s.l.), and from the MWR and the Raman lidar belonging to the Institute of Earth Sciences (ICT) and Earth Remote Sensing Laboratory (EaRSLab) in Évora (Portugal) (38.568°N, 7.912°W, 293 m a.s.l.), both ACTRIS (Aerosol, Clouds and Trace Gases Research Infrastructure) stations (AGORA and EVASO observational facilities, respectively), as well as data from radiosondes launched from Graciosa island (Azores, Portugal) (39.053°N, 28.010°W, 26 m a.s.l.)) and La Jolla (California, USA) (32.897°N, 117.257°W, 7 m a.s.l.). Table 1 summarizes the information of the aforementioned stations and Figure 1 shows their location on a map.

Table 1. Ground stations and instruments used in this study.

Facility	Location and Altitude	Instruments
Andalusian Global Observatory of the Atmosphere (AGORA)	Granada (Spain) 37.164°N, 3.605°W, 680 m a.s.l.	Ceilometer MWR
Evora Atmospheric Sciences Observatory (EVASO)	Évora (Portugal) 38.568°N, 7.912°W, 293 m a.s.l.	Lidar MWR
Eastern North Atlantic (ENA)	Azores (Portugal) 39.053°N, 28.010°W, 26 m a.s.l.	Radiosondes
Eastern Pacific CAPE (EPC)	La Jolla (California, USA) 32.897°N, 117.257°W, 7 m a.s.l.	Radiosondes

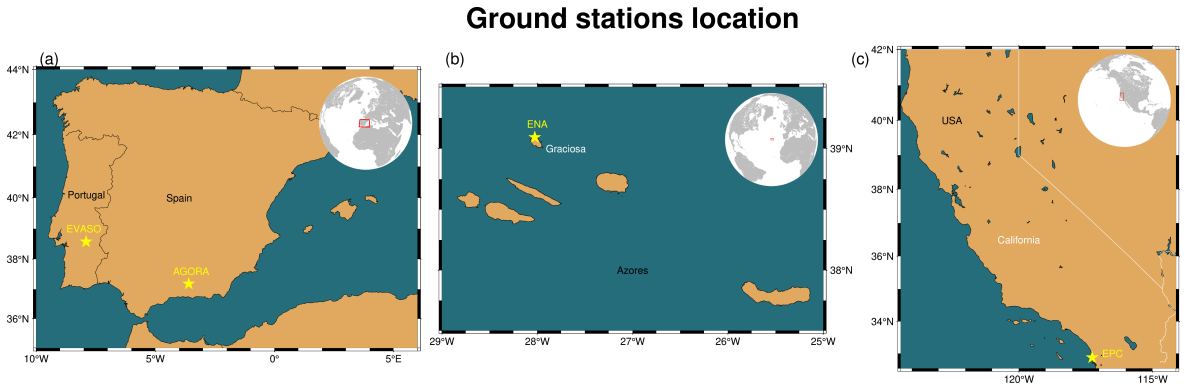

Figure 1. Location of the measurement stations used in this work, marked with a yellow star. (**a**) Stations in the Iberian Peninsula. (**b**) Station in Azores (Portugal). (**c**) Station in California (USA).

2.1.1. COSMIC-2

Each COSMIC-2 satellite is equipped with the advanced TGRS (GPS, GALILEO and GLONASS (TriG) Global Navigation Satellite System (GNSS)-RO Receiver System) receiver, developed by the Jet Propulsion Laboratory (JPL), which belongs to the National Oceanic and Atmospheric Administration (NOAA) [49]. It includes a high-gain beam-forming RO antenna that achieves the best signal-to-noise ratio in RO measurements to date (>2500 V/V in a 1 Hz band) [44]. The TGRS is able to provide high-quality cross sections of the Earth's atmosphere. The resulting RO data can be inverted to obtain information about temperature, pressure, humidity, and lighting formation. Also, it measures electron density and flashes of light originating from particles passing through the upper atmosphere, a phenomenon known as scintillation. Esterhuizen et al. [50] describe the architecture and the implementation of the receiver, as well as the results obtained with a prototype, showing the key issues related to the next generation of spatial receivers.

In addition to the TGRS, each satellite has an ion velocity meter (IVM) and a radio beacon. The former is an instrument that measures the velocity of electrons in the upper atmosphere, a fundamental metric for space weather predictions and to estimate the concentration, composition and temperature of electrons. Moreover, these parameters provide information about the effects of geomagnetic and solar storms in the atmosphere. The radio beacon measures the total content of electrons in the upper atmosphere, useful information for monitoring the space weather.

COSMIC-2 satellites orbit at a height of 720 km above the Earth's surface with a (low) inclination angle of 24°. The latter feature restricts the occultations to locations between 45°S and 45°N, even though a high percentage of these are found in intertropical latitudes (see Figure 2 of Ho et al. [51]), allowing a high time–space density of atmospheric profiles in an area of interest for studies about genesis, development and evolution of hurricanes, among other phenomena. Furthermore, since the six satellites are evenly arranged in space, the COSMIC-2 mission provides a regular coverage of observations that weather balloons and ground stations cannot reach, especially over oceans and other traditionally data-scarce regions.

Since its launch, the COSMIC-2 mission has provided more than 4000 high-quality atmospheric profiles per day. The COSMIC Program counts on a series of telecommunication link stations to receive data from the satellites and send them to the COSMIC Data Analysis and Archive Center (CDAAC) for processing. This network of surface stations ensures that the data products are available in near-real time so that they can be used for numerical weather prediction.

The CDAAC makes use of a data processing package to turn the fundamental observable, i.e., phase delay, into vertical profiles of bending angle, refractivity, temperature and humidity. As summarized by Ho et al. [51], this inversion procedure includes (i) the precise determination of the orbit and clocks synchronization to remove the geometric Doppler effect and to correct the relative movement between the GNSS satellite and the

COSMIC-2 satellite, (ii) the conversion of the Doppler effect into bending angle (refraction angle), (iii) the extrapolation of the ionospheric correction to the lower troposphere, necessary because of the influence of the ionosphere on the measurement of the phase delay of GPS signals, (iv) the initialization of the Abel transform that converts bending angles into refractivity profiles, (v) a variational algorithm to invert profiles of refractivity into profiles of temperature and moisture in the troposphere and lower stratosphere, and (vi) a quality control to distinguish acceptable from unacceptable data. A more detailed description of the inversion procedure, including implementation methodologies and validation analysis, can be found in Kuo et al. [52] and Ho et al. (2009 and 2012) [53,54].

Refractivity (N) is an optical magnitude that depends on the refractive index of the medium. It informs about the ability of the medium to produce refraction. In the atmospheric context, the term refractivity specifically refers to the ability of the atmosphere to bend light, or any electromagnetic wave, as a result of air density variations along the vertical profile. Within the troposphere, refractivity can be formulated as a function of temperature, pressure, and water vapor pressure according to the equation [39]:

$$N = 77.6 \frac{p}{T} + 3.73 \cdot 10^5 \frac{e}{T^2} \quad (1)$$

where p is the atmospheric pressure in hPa, T is the temperature in K, and e is the water vapor pressure in hPa. It is worth mentioning that for ionospheric studies, a term accounting for electron density should also be taken into account.

CDAAC uses a one-dimension variational method (1D var, https://cdaac-www.cosmic.ucar.edu/cdaac/doc/documents/1dvar.pdf, last accessed on 14 February 2024) to obtain temperature, humidity, and pressure profiles from refractivity profiles, essentially. CDAAC also makes available another product (wetPf2 profiles) in which ancillary information of the lower troposphere (for example, from the European Centre for Medium-Range Weather Forecasts (ECMWF)) is assimilated into the moisture retrieval procedure [55]. In this way, the impact of refractivity bias on water vapor retrievals due to possible super-refraction conditions is reduced.

The wetPf2 profiles were employed in this work, whose data are freely available on the COSMIC-2 website (https://www.cosmic.ucar.edu/what-we-do/cosmic-2/data, last accessed on 15 March 2024). This dataset contains vertical profiles (referenced to height above mean sea level) of pressure, water vapor pressure, temperature, refractivity, longitude, and latitude, with a vertical resolution of 50 m up to tropopause and 100 m at higher levels. The study covers the first 4 years of COSMIC-2 data: from 1 October 2019, to 30 September 2023. During this period, 46 COSMIC-2 profiles were found near Granada, 182 profiles were located near Évora, 168 were close to Graciosa, and 72 were located near La Jolla. The criterion to define a COSMIC-2 profile as near a ground station depended on whether their horizontal distance was less than 100 km, which is a threshold commonly used when intercomparing satellite observations with ground station measurements [56]. As the latitude and longitude vary along the profile, there are no unique coordinates for a single profile. Given that the focus of this study is the ABLH, normally situated in the first kilometers, the mean values of latitude and longitude from surface level up to 4 km were chosen as the representative coordinates for each profile. Apart from the geographical position, an additional condition was required to take a profile into the analysis: its minimum height should be below 500 m to reduce the risk of overlooking the true level of the ABLH [45,57]. In addition to the difficulty of the radio-occultation technique to sound the atmosphere in complex-topography zones, this imposition could significantly reduce the amount of available data over mountains. Thus, when averaging, results should be taken with caution over mountain ranges, as well as over the borders of the spatial domain ($\pm 45°$) since the number of profiles might be insufficient to analyze the average behavior.

2.1.2. Microwave Radiometers

The microwave radiometers (MWR) employed in this study are RPG-HATPRO systems (Radiometer Physics GmbH), second generation in the case of Granada and fourth generation for that installed in Évora. Both are part of the MWRnet network (http://cetemps.aquila.infn.it/mwrnet/members.html, last accessed on 14 April 2024) [58]. They measure the brightness temperature with a radiometric resolution of between 0.25 and 1 K root mean square error and with an integration time of the order of one second. More concretely, they capture the atmospheric radiation in the 51–58 GHz band (oxygen—V band) for temperature profile inversion and the 22–31 GHz band (moisture—K band) for moisture profile inversion. Then, the inversion algorithms convert the radiance observed in a certain frequency band into temperature and humidity profiles. Such inversion algorithms are widely described by Rose et al. [58]. The resulting profiles span from the ground up to 10 km, dividing the atmosphere into 93 levels. The vertical resolution gradually decreases along the profile, from 20–30 m in the first hundred meters to about 200 m in the upper troposphere. The temporal resolution is of the order of one minute. Moreover, the MWRs include sensors to measure the pressure, temperature, and relative humidity at the surface, among other variables. The MWR in Granada has routinely been active since November 2010 at AGORA, whereas the MWR in Évora has been operational since October 2014 at EVASO. Further information about these instruments can be found in the work of Vaquero-Martínez et al. [59].

2.1.3. Ceilometer and Lidar

The vertical profiling systems used for aerosol particles are different at the Granada and Évora stations. While in Granada the instrument employed is a ceilometer, in Évora, a Raman lidar is utilized.

The ceilometer installed in Granada is a CHM15k that operates with a pulsed Nd:YAG laser of 1064 nm. The energy per pulse is 8.4 μJ, and its repetition frequency is within the range of 5 to 7 kHz. The divergence of the laser beam is lower than 0.3 mrad. The backscattered signal is captured by a telescope whose field of view is 0.45 mrad. Such signals are then detected by an avalanche photodiode in photon-counting mode. Full overlap between the telescope's field of view and the laser beam is achieved at about 1500 m above the instrument [60]. According to the overlap function provided by the manufacturer, 90% of the overlap occurs between 555 and 885 m above the instrument. This device has been working at AGORA since November 2012 and is part of the ICENET network [61], included in E-PROFILE (European Profile of the European Meteorological Network).

In Évora, a PollyXT Raman lidar system [62] known as PAOLI (Portable Aerosol and Cloud Lidar) runs with 3 elastic channels (355, 532, and 1064 nm), 2 inelastic channels (387 and 607 nm), and a sixth channel of perpendicular polarization (532 nm). It provides continuous measurements of the vertical distribution of aerosols and clouds with high vertical and temporal resolution [63]. In this case, the overlap function affects heights below approximately 800 m, approximately. A detailed description of the technical characteristics of this instrument can be consulted in Preißler et al. [64]. PAOLI has regularly operated since September 2009. This lidar system belongs to the EARLINET (European Aerosol Research Lidar Network) [65] and SPALINET (Spanish and Portuguese Aerosol Lidar Network) networks [66].

Ceilometers and lidars measure the range-corrected signal (RCS), which is proportional to the attenuated backscatter coefficient (β_{att}). The definition of RCS derives from the elastic lidar equation, formulated as follows:

$$P(R,\lambda) = K\,\frac{O(R)}{R^2}\,\beta(R,\lambda)\,T^2(R,\lambda) \tag{2}$$

where $P(R,\lambda)$ is the power measured by the detector for a wavelength λ at a vertical distance R; K is a constant that accounts for the power emitted by the laser, the speed of light, the duration of the emitted pulse, the quantum efficiency of the detectors, and the

effective detection area of the telescope; $O(R)$ is the overlap function that depends on the overlap between the telescope's field of view and the laser beam; $\beta(R, \lambda)$ is the backscatter coefficient; and $T(R, \lambda)$ is the atmospheric transmissivity. Regrouping terms leads to the appearance of the RCS in the equation:

$$RCS(R, \lambda) = P(R, \lambda)\, R^2 = K\, O(R)\, \beta(R, \lambda)\, T^2(R, \lambda) = K\, O(R)\, \beta_{att}(R, \lambda) \quad (3)$$

The vertical resolutions of the RCS profiles obtained by the ceilometer and the lidar are 15 and 30 m, respectively, whereas the temporal resolutions are 15 and 30 s, respectively [63].

2.1.4. Radiosondes

The radiosoundings whose data are used in this study are run by the Atmospheric Radiation Measurement (ARM) Program (https://www.arm.gov/, last accessed on 14 April 2024), developed by the United States Department of Energy. In particular, radiosondes over Graciosa are operated by the Eastern North Atlantic (ENA) observatory, which was established in 2013 as the latest permanent measurement station of the ARM Program to date. In La Jolla, there is a mobile facility known as EPC (Eastern Pacific CAPE) that has been framed in the Eastern Pacific Cloud Aerosol Precipitation Experiment (EPCAPE) since the beginning of 2023.

ARM observatories have been adopting the most cutting-edge technology in radiosondes developed by Vaisala. The ARM facility was the first to employ the advanced H-Humicap sensor in RS80 radiosondes, the first one to make the transition towards the family of RS90 family with dual-Humicap sensors, and the pioneer in using the RS92 family. These devices are able to retrieve vertical profiles of pressure (resolution: 0.1 hPa; uncertainty: 0.5 hPa), temperature (resolution: 0.1 K; uncertainty: 0.5 K), and relative humidity (resolution: 1%; uncertainty: 5%). The temporal and vertical resolutions depend on the ascent rate of the balloon, which is commonly between 5 and 5.5 m/s. See the handbook [67] for a thorough description of all the characteristics of the radiosoundings operated by ARM.

The radiosondes launched at ENA and EPC observatories retrieve meteorological information on the vertical column including pressure, temperature, and relative humidity. The vertical resolution is normally about 5 m, but it actually depends on how fast the balloon ascends. Radiosoundings over Graciosa and La Jolla are typically launched twice a day and at regular times: usually one around noon and another at midnight.

2.2. Methodologies to Retrieve ABLH

Objectively quantifying the performance of a method to truly detect ABLH is often challenging, especially because there is no global technique that can serve as verification. Thus, the goodness of an algorithm is assessed by intercomparisons with multiple methodologies. Moreover, when comparing results, possible disagreements can occur not only because of the uncertainties in the methods themselves but also due to methodological and technical aspects, such as the spatial and temporal resolution of each instrument. Another source of discrepancy may arise when comparing results obtained from methodologies with different observed quantities, e.g., thermodynamic methods against aerosol-based methods since their principles are not the same.

Analysis should be especially thorough when several sublayers are present. This tends to happen during night and early morning, when the RL and the SBL coexist simultaneously. The boundaries between the SBL and the RL, and between the RL and the FT, can exhibit similar characteristics, which is a potential problem hardly manageable for automated computational algorithms. Uncertainties might also increase when changes occur in ABL dynamics: sunrise, sunset, low-level jet, advection, clouds, or fog. In such situations, atmospheric profiles often exhibit various boundary layers, whose identification can be challenging.

In this work, several methods are applied to estimate the ABLH. Each involves one atmospheric variable: refractivity, temperature or RCS, whose vertical profiles were obtained

through the experimental devices described in Section 2.1. Then, the ABLHs retrieved from COSMIC-2 refractivity data are compared to those computed using other data sources to find an ABLH-estimator algorithm that maximizes the agreement between methodologies. The next subsections detail the basis of the methods employed.

2.2.1. Methods Based on Refractivity

Refractivity tends to decrease with height, revealing a strong negative gradient at the top of the ABL, which is associated with a significant reduction in temperature and moisture [16,29]. For that reason, ABLH is traditionally identified as the height where the absolute minimum refractivity gradient (MRG) is found [30]. However, Santosh [45] emphasized that processes in the ABL do not demand the refractivity gradient to exhibit its absolute minimum at the top but rather a significant minimum since other factors can produce substantial changes in the refractivity profile. In the lower troposphere, refractivity is highly sensitive to changes in water vapor content, rather than changes in temperature [6]. Thus, the presence of clouds or moisture advection can cause negative peaks in the refractivity gradient profile whose strength can be similar, or even greater, than that at the ABL top, which leads to ambiguous attribution when identifying the ABLH. This problem is well known [29,30,48].

Santosh [45] conducted an ABLH study under instability conditions, independent of the refractivity profile shape. They proposed not to ignore significant negative peaks below the MRG, an approach that they called lowest significant gradient (LSG). By using radiosounding data in Central India and over the tropical Indian Ocean, they concluded that the best agreement between ABLHs computed from refractivity data and those estimated through the Liu and Liang method (which was chosen as reference; see Section 2.2.2) came to pass when the ABLH was defined as the height where a negative peak in the refractivity gradient profile (below the MRG) had a magnitude of, at least, 80% with respect to the MRG. In the case where more than one peak fulfills the conditions, the lowest one is considered the ABLH. If there are no peaks below the MRG that reach the required magnitude, the method coincides with the traditional one, and so the ABLH is attributed to the height where the MRG occurs.

In this work, the refractivity gradient (N') is calculated using the second-order central differences approach [68]. So, the refractivity gradient at a height z_i (i is the index for values in the height profile) is:

$$N'(z_i) = \frac{(z_i - z_{i-1})^2 N(z_{i+1}) + (z_{i+1}^2 - z_{i-1}^2 - 2z_i(z_{i+1} - z_{i-1}))N(z_i) - (z_i - z_{i-1})^2 N(z_{i-1})}{(z_i - z_{i-1})(z_{i+1} - z_i)(z_{i+1} - z_{i-1})} \quad (4)$$

If data are evenly spaced (i.e., $z_{i+1} - z_i$ is a constant) as is the case in the COSMIC-2 data in the first kilometer, then the equation adopts a much simpler form:

$$N'(z_i) = \frac{N(z_{i+1}) - N(z_{i-1})}{z_{i+1} - z_{i-1}} \quad (5)$$

MWR and radiosondes do not directly provide refractivity profiles, so they must be calculated using Equation (1). However, this formula cannot be directly applied since not all variables are known. MWR outputs provide temperature and absolute humidity (ρ_v) profiles. The water vapor pressure can be easily computed from the ideal gas law for water vapor:

$$e = \rho_v R_v T \quad (6)$$

where R_v is the specific gas constant for water vapor and equals 461.5 J/kg·K. To retrieve the atmospheric pressure profile, the hydrostatic equation (Equation (7)) and the ideal gas law for dry air (assuming that virtual temperature, T_v, is approximately equal to temperature; Equation (8)) are combined to obtain Equation (9):

$$dp = -\rho\, g\, dz, \quad (7)$$

$$p = \rho\, R_d\, T_v \approx \rho\, R_d\, T, \tag{8}$$

$$p(z) = p_0 \exp\left(-\frac{g}{R_d}\int_0^z \frac{1}{T(z')}\, dz'\right) \tag{9}$$

where ρ is the air density, g is the gravitational acceleration, z is the vertical coordinate (height), R_d is the specific gas constant for dry air (287.05 J/kg·K), and p_0 is the atmospheric pressure at surface. The integral in Equation (9) was computed using the composite Simpson's rule [69].

On the other hand, radiosounding data do contain a profile of pressure but not of water vapor pressure. The water content is instead recorded in a relative humidity (U) profile. The relative humidity is related to the water vapor pressure by the equation:

$$U = 100\,\frac{e}{E} \tag{10}$$

where E is the saturation vapor pressure, which exclusively depends on temperature. Its value is computed using the empirical formula [70]:

$$E(T) = 6.107 \exp\left(\frac{a\,(T(z) - 273)}{b + (T(z) - 273)}\right) \tag{11}$$

where the values of a and b are 17.18 and 245.4 K, or 17.08 and 234.2 K, respectively, depending on whether T is lower or greater than 273 K.

Once the three variables (i.e., T, p, and e) are available, the Equations (1) and (4) can be used to estimate the ABLH. Moreover, to refine the method, the Savitzky–Golay filter [71] is applied to the refractivity gradient profile using a one-order polynomial and a window filter length of 5 points for the profile from MWR data, and 25 points for that one from radiosounding data. Additionally, only those negative peaks with half-width prominence of at least 2 times the vertical resolution are considered. These refinements help to dismiss spurious or insignificant peaks.

2.2.2. Methods Based on Temperature

Algorithms to estimate ABLH from temperature profiles usually distinguish between stable and unstable conditions [10]. Nevertheless, the methods used to detect the ABLH under stable situations often refer to the top of the SBL (instead of the RL, which is sometimes not considered an ABL layer). For that reason, temperature-based approaches are only applied in cases of instability (and neutrality, depending on the technique), when the definition of the upper limit of the ABL is not a matter of disagreement.

The determination of the regime type (stable or unstable) is not universal either. According to Liu and Liang [7], the state of the atmosphere is identified by assessing the difference of potential temperature between 150 and 10 m above ground. Over land, the conditions are considered unstable if such a difference is less than -1 K, whereas over oceans, that threshold is -0.2 K. However, if the difference in potential temperature is greater than $+1$ K and $+0.2$ K, respectively, then the regime is considered stable. Intermediate situations are classified as neutral. On the other hand, de Arruda Moreira et al. [72] define a situation as unstable if the potential temperature at the surface is higher than the potential temperature at any point of the vertical profile, up to 5 km.

In any case, the first step to retrieve the ABLH from a temperature profile is to calculate the potential temperature (θ) profile. This can be achieved through the Stull's approximation [73]:

$$\theta(z) = T(z) + \gamma_d\, z \tag{12}$$

where z is the height above sea level, and γ_d is the adiabatic temperature gradient for dry air with a value of 9.8 K/km.

Following the methodology used by de Arruda Moreira et al. [72], the ABLH under unstable conditions is given by the parcel method (PM), which identifies the ABLH as the

height to which a parcel of air at ambient temperature can adiabatically rise from ground because of convection [20,74]. This is equivalent to saying that the ABLH is the height where the potential temperature is equal to that at the surface. However, the Liu and Liang method [7] formulates two requisites to be fulfilled to assign the ABLH under conditions of instability or neutrality that depend on the surface type (land or ocean). Firstly, the potential temperature at ABLH must be 0.5 K higher than at the surface over land, and 0.1 K higher over oceans. Secondly, the potential temperature gradient must be, at least, 4 K/km over land, and 0.5 K/km over oceans. The ABLH is the lowest height where both requirements are reached.

2.2.3. Method Based on RCS

The time–space distribution of aerosol particles and moisture is normally a result of a complex combination of processes including emission, formation, accumulation, deposition, transport, and mixing. For that reason, the attenuated backscatter coefficient profiles record, in a certain way, the recent history of the ABL dynamics, using atmospheric aerosols as tracers. Then, boundary layers within the atmosphere can be detected if aerosol properties change among layers. The most noticeable variation tends to occur at the ABL top since the aerosol concentration and moisture are usually significantly higher in the ABL than in the FT [10].

Hence, methods to retrieve ABLH from aerosol measurements are based on detecting regions where a significant vertical (and sometimes also temporal) decrease in the attenuated backscatter coefficient, or its gradient, is produced. That said, ABLH detection becomes more difficult if multiple layers are present. There are several methodologies to retrieve ABLH from aerosol particle profiles. In this work, the gradient method [75] is employed. The first step is to find out if there are decoupled layers above the ABL, which can be identified if the aerosol properties differ. These layers are represented by a local increase in RCS or by a positive region in the RCS gradient profile. According to the gradient method, in cases where no decoupled layers are detected, the ABLH is simply assigned to the height where the absolute minimum of the RCS gradient is found. However, if coupled layers are recognized, the ABLH is assigned to the negative peak located at the highest altitude in the first negative derivative zone. It is important to note that for the automatic computation of the ABLH, it was convenient to smooth the RCS and RCS gradient profiles. This was achieved by the application of the Savitzky–Golay filter, using a one-order polynomial and setting to 5 points the length of the filter window for the RCS profile and 9 points in the case of the RCS gradient profile.

As a summary, Table 2 shows the main aspects of the methodologies to calculate the ABLH described in this section.

Table 2. Methodologies employed to calculate the ABLH, including the atmospheric variables, the data sources, the methods and equations used, and the subsection in which each method is explained.

Atmospheric Property	Instrument (Variables)	Method	Equations	Section
Refractivity (N)	COSMIC-2 satellite (N) MWR (T, ρ_v, p_0) Radiosonde (T, p, U)	MRG [28] LSG [45]	(4) (1), (4), (6), (8), (7), (9) (1), (4), (10), (11)	Section 2.2.1
Potential temperature (θ)	MWR (T) Radiosonde (T)	PM [74] Liu and Liang [7]	(12)	Section 2.2.2
Range-corrected signal (RCS)	Ceilometer (RCS) Lidar (RCS)	Gradient [75]	(4)	Section 2.2.3

2.3. Determination of the Optimum Algorithm for ABLH Retrieval from COSMIC-2 Data

Santosh [45] considered that significant peaks below the MRG could represent the ABLH. They carried out a study assigning the diurnal ABLH to the lowest peak whose magnitude was at least 60, 70, 80, and 90% of MRG. They found that the use of the 80%

threshold led to the best agreements with the Liu and Liang method [7]. Figure 2 illustrates the ABLH determination method presented by Santosh [45]. In this work, the search for the best algorithm also focuses on polishing this percent parameter (hereafter denoted by τ). However, we introduce substantial new aspects to the study.

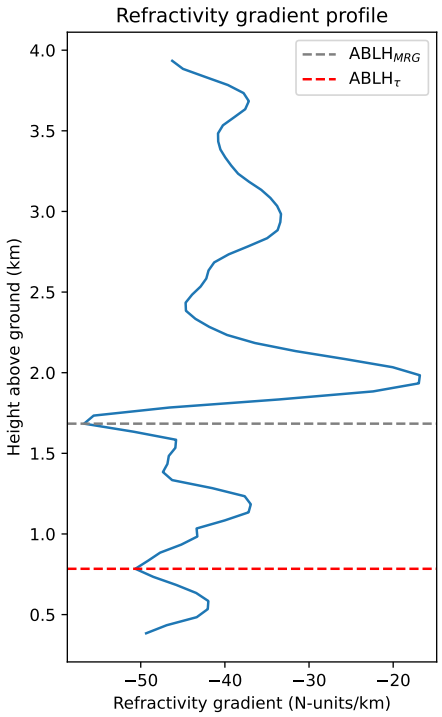

Figure 2. Example of the ABLH determination from a refractivity gradient profile according to Santosh's method. The dashed line in grey indicates the peak with minimum magnitude (MRG method; $ABLH_{MRG}$). The ABLH is attributed to the lowest negative peak whose absolute magnitude is at least 80% that of the MRG peak (dashed line in red; $ABLH_{\tau}$).

In order to perform consistent comparisons, not only must a COSMIC-2 profile be spatially near a ground station, but also both measurements should be nearly synchronous. So, the maximum time allowed between a COSMIC-2 profile and a MWR or lidar observation is set to 15 min. Given the high temporal resolution of these systems, 30 min averaged profiles, centered at the time of the COSMIC-2 profile, are computed for temperature, humidity, and RCS data to remove possible irregularities in single profiles. Regarding radiosounding data, their low temporal resolution requires broadening the temporal range to 30 min. The spatial and temporal constraints limit the number of comparable observations. Moreover, since the characteristics of the ABL vary over the day and over different surface types [76], the analysis distinguishes three phases throughout the day: daytime, nighttime, and transition periods (sunrise and sunset), and a differentiation between land and oceanic zones is made. Then, a τ value is estimated for each situation. Sunrise and sunset times are calculated from the geographical coordinates and the day of the year. The duration of the transition intervals is set to 3 h, centered at the sunrise/sunset time. Data from the stations in Granada and Évora are used for determining the optimal τ over land, whereas data from facilities in Graciosa and La Jolla are considered highly ocean-influenced and therefore used for validation over oceans.

The degree of agreement between COSMIC-2 ABLHs and those from other methodologies is quantified by robust linear regressions. The inclusion of a robust configuration responds to the scarcity of comparable profiles and the high sensitivity of 'simple' linear regressions to outlier values. The robustness in the analysis consists of casting aside those points in a scatter plot whose distance to the identity line is greater than twice the standard deviation of all the distances. The possible values considered for τ range from 50 to

100%, with 1%-step. The choice of the best τ is based on a goodness-of-fit function (GF, Equation (13)) that takes into account the correlation coefficient (R), the slope (m), and the number of observations (n) considered in the linear regression. The Gaussian form of the GF function ensures higher values are returned as R and n increase and m approaches one. The reader may note that if n tends to a very large number, the GF function will become very insensitive to m, so this dependency should be eliminated for large database studies. In the event of obtaining consecutive equal maximum GF outputs, the mean value is considered optimal τ.

It is worth recalling that τ has no physical meaning. Hence, it could be biased due to the methodology employed, as well as the location where the comparative analysis is conducted. For that reason, it is convenient to use diverse techniques and different sources of data. Furthermore, the different vertical resolutions among the instruments could imply that the optimal value for τ depends also on the specific system employed, that is, best agreements between two refractivity-based methodologies could happen when using two distinct τ values, respectively.

$$GF(R, m, n) = R \exp\left(\frac{-(m-1)^2}{n}\right) \quad (13)$$

3. Results

3.1. Tune-Up of the ABLH Retrieval Algorithm

The results of the analysis to determine the optimal τ are represented in the form of a matrix, whose elements are the values of the GF function resulting from the comparison between the ABLHs estimated through COSMIC-2 data and those calculated by another methodology and dataset. Given the large number of outputs, and for reasons of illustration in this manuscript, results are depicted here considering τ values with a step of 5%. The following subsections describe the results for land and oceanic regions separately.

3.1.1. Land Regions

Figure 3 displays the GF values resulting from comparisons with data collected by means of the MWRs, the ceilometer, and the lidar installed in Granada and Évora, respectively, for each period considered throughout the day. Data from these stations are used to find the best τ value over continents. For daytime, best agreements are achieved when comparing with lidar data, with GF maximum when τ equals 82% (GF = 0.828). For nighttime, the optimal τ is also obtained through lidar data, and drops to 68% (GF = 0.813). Finally, for transitions between day and night, and vice versa, the optimal value of τ is 98% (GF = 0.956), which is validated by ceilometer data. This value is almost the same as the traditional method, which equates to using $\tau = 100\%$.

The degree of agreement may depend on the phase of the day, although it could be partially masked by the use of a robust method. Even so, worse agreement is generally observed at the night phase, surely owing to the more complex structure of the ABL [10] because of the appearance of sublayers within. During nighttime, the presence of the SBL might cause relatively strong peaks in the refractivity gradient which may hinder the application of the algorithm [45]. Moreover, temperature-based approaches (PM and Liu and Liang method) cannot be applied during this period, as there are barely any instability cases. The night situation mostly contrasts with that observed during daytime, when the ABL tends to show its simplest form, exhibiting a prominent refractivity peak at the transition between the ABL and the FT [77,78].

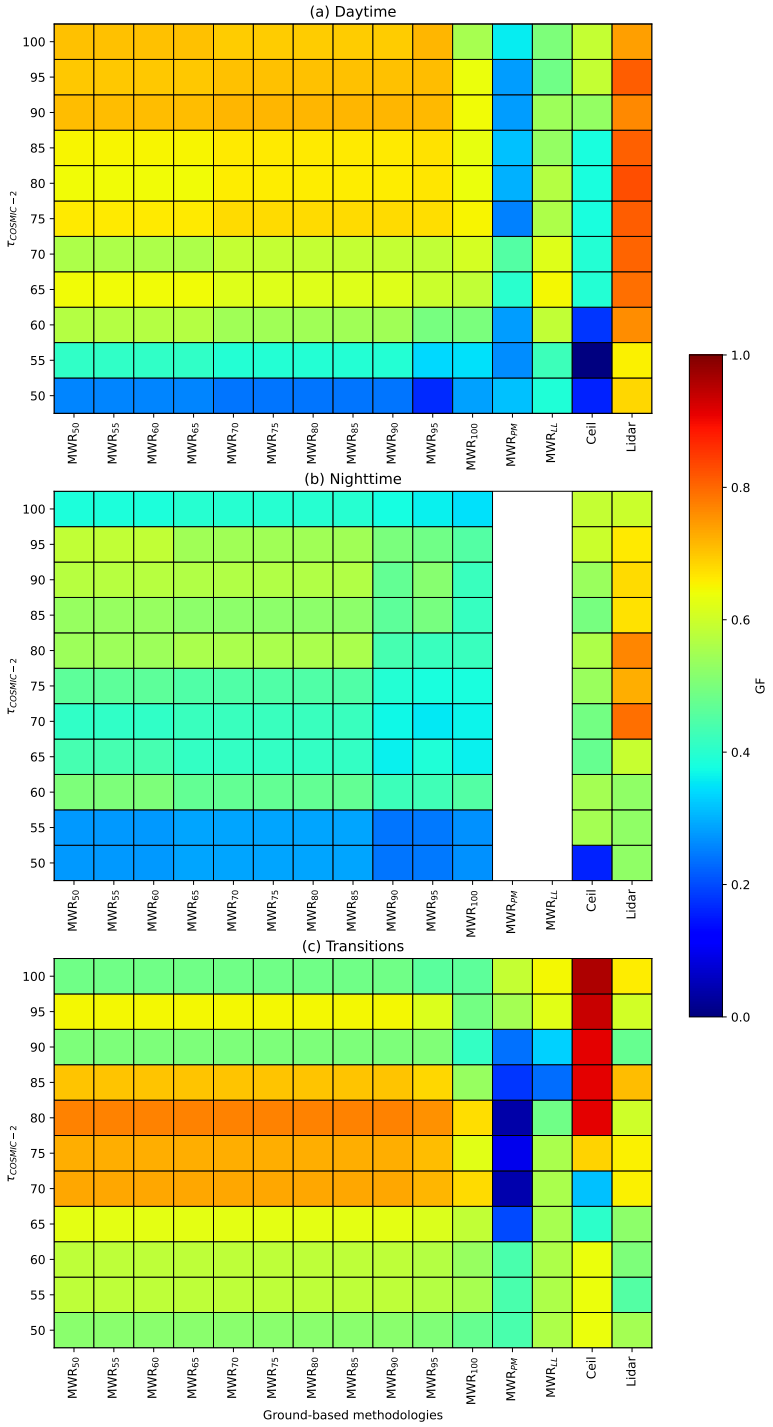

Figure 3. Values of the GF function resulting from comparing the ABLHs obtained through COSMIC-2 refractivity data with those computed from data collected in the Granada and Évora stations. (**a**) GF values for daytime. (**b**) GF values for nighttime. (**c**) GF values for transition periods (sunrise and sunset). The vertical axis refers to the τ value used in COSMIC-2 data. The horizontal axis corresponds to the validation methodologies: MWR_x: refractivity method from MWR data using x% as τ value; MWR_{PM}: parcel method applied to MWR data; MWR_{LL}: Liu and Liang method applied to MWR data; Ceil: gradient method applied to RCS data from ceilometer; Lidar: gradient method applied to RCS data from lidar. Blank cells inform of the non-availability of data to carry out the comparison.

3.1.2. Oceanic Regions

Radiosondes are normally launched twice a day at fixed times, which strongly restricts the number of comparable observations with other data sources. Additionally, no radiosounding data cover the sunrise and sunset periods. Given the low amount of comparable measurements (≈10) and considering that oceanic ABL presents a rather subtle daily evolution [6], only one τ value is calculated for the entire day. Moreover, because the number of instability cases (<5) is considered insufficient and not representative, the methods based on temperature are not applied. Thus, the election of the optimal value of τ relies on the method based on refractivity.

Figure 4 depicts the resulting GF values from comparing ABLHs estimated through COSMIC-2 refractivity data with ABLHs calculated from radiosounding data collected at ENA and EPC observatories. The comparative analysis reveals an optimal τ value of 99% (GF = 0.984) for oceanic regions. Such best agreement is achieved when using τ = 50% in the validation methodology, i.e., in the refractivity gradient profile from radiosounding data. That difference of τ values is attributed to the difference in vertical resolutions of the systems involved. While COSMIC-2 data are profiled with a constant vertical resolution of 50 m for altitudes of a few kilometers, ARM radiosondes collect data every about 5 m. In other words, there is a difference of one order of magnitude. When using a coarser resolution, strong refractivity gradient peaks may not be well captured or become smoothed, owing to interpolation or averaging procedures so that their magnitude is not that prominent with respect to other weaker peaks. Consequently, a higher τ is necessary in comparison with finer-resolution profiles. Table 3 summarises the findings described in this section, including the optimal τ values for both land and oceanic regions and information about their validation.

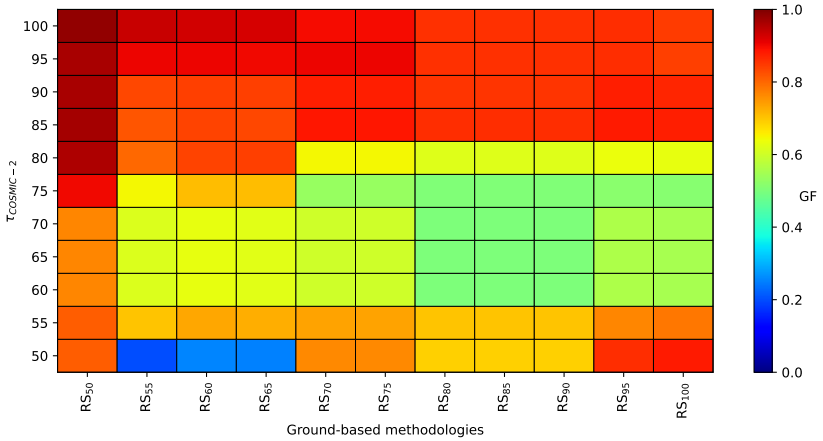

Figure 4. Values of the GF function resulting from comparing ABLHs obtained through COSMIC-2 refractivity data with those computed from data collected in ARM stations. The vertical axis refers to the τ value used in COSMIC-2 data. The horizontal axis corresponds to the validation methodologies: RS_x: refractivity method from radiosounding data using x% as τ value.

Table 3. Tuned τ values for land areas according to the day phase, and optimal value for oceanic regions. Additionally, the data source for each validation, as well as the GF value and the number of observations considered, are indicated.

Surface	Period	τ (%)	Validation Data Source	GF	*n*
Land	Daytime	82	Lidar	0.828	21
	Nighttime	68	Lidar	0.813	18
	Transitions	98	Ceilometer	0.956	9
Ocean	-	99	Radiosonde	0.984	8

3.2. ABLH Seasonal Fields from Satellite Observations

Figure 5 shows the seasonal mean fields (December, January and February (DJF); March, April and May (MAM); June, July and August (JJA); September, October and November (SON)) of ABLH (above ground level), for the spatial domain covered by COSMIC-2 mission, and gridding to 1°×1° resolution. The ABLH is estimated utilizing the algorithm proposed in Section 3.1, which is applied to refractivity data from the COSMIC-2 mission considering the period from October 2019 to September 2023. The resulting patterns seem to be primarily modulated by the latitude and the underlying surface type. Seasonal variations may directly originate from the modifications in the incoming solar radiation throughout the year due to the changes in the solar declination angle which defines seasons. Surface properties, like heat capacity, also play an essential role. In this respect, it is important to bear in mind that water has a high specific heat capacity (4184 J/kg·K) in comparison to normal values found in surface continental regions (ranging from 800 to 1700 J/kg·K, depending on land characteristics and humidity [79]). This causes surface air convection to be favored over land (hotter than sea surface), among other implications. As a result, the seasonal cycle is generally more pronounced over land than over oceans. Figure 6 depicts the quantification of ABLH variability through standard deviation for the whole period, and the seasonal amplitude, defined as the difference between the ABLH mean fields during JJA and DJF. Both maps effectively show that high-variability zones are generally located over land.

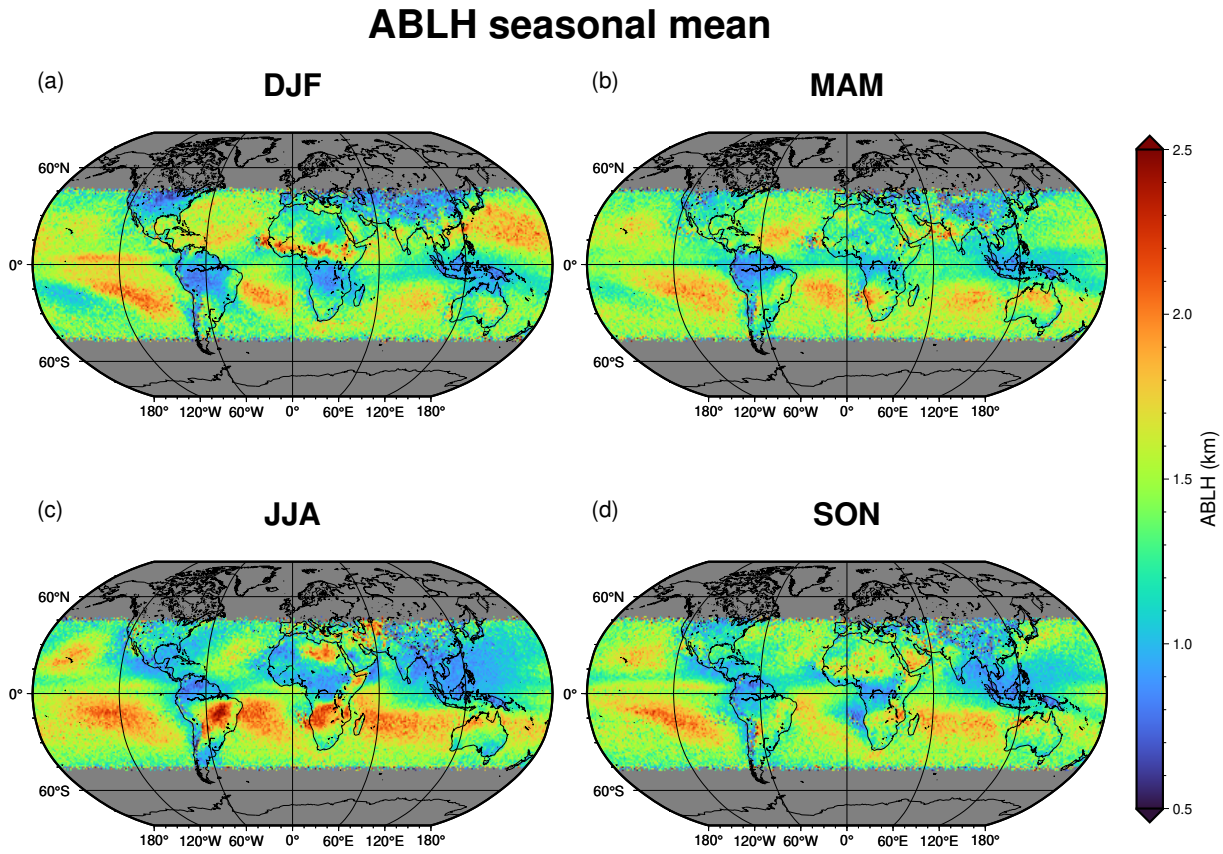

Figure 5. Seasonal mean fields of ABLH above ground level resulting from applying the algorithm derived in Section 3.1 to refractivity data of COSMIC-2 mission. Each subpanel refers to one season: (**a**) December, January, and February (DJF); (**b**) March, April, and May (MAM); (**c**) June, July, and August (JJA); (**d**) September, October, and November (SON). Locations in latitudes beyond ±45° are out of the COSMIC-2 spatial domain.

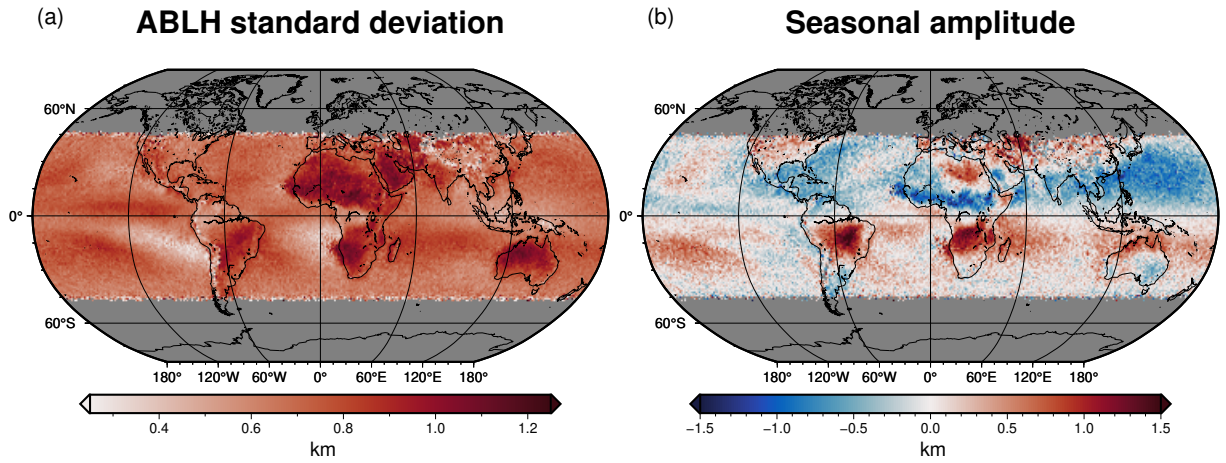

Figure 6. Quantification of the ABLH variability. (**a**) Standard deviation considering the whole period. (**b**) Seasonal amplitude: difference between the mean ABLH field in JJA and DJF. Locations in latitudes beyond ±45° are out of the COSMIC-2 spatial domain.

Overall, ABLH on average is deeper over oceans than over land. However, the highest values are found over continental zones. This is explained by the less pronounced daily cycle over oceans because of the lower surface temperature amplitude [4,7]. That said, the highest ABL tops are produced over locations within latitudes between 5°S and 20°S (land and ocean) during the JJA period (boreal summer or austral winter), where ABLH exceeds 2 km in many points. Maxima are indeed found over land areas in Africa and notably concentrated in the center of Brazil, where ABLHs can exceed heights of 2.5 km above ground level. Other high ABLHs over land are identified in a region belonging to Egypt and Libya in the JJA period, and along a narrow strip around 3°N, between the Sahel and the equator during DJF. Both places present ABLHs of about 2 km. On the other hand, low ABLHs tend to occur over the equator in MAM and SON, and in its vicinity during the rest of the year, above or below this line depending on the season (JJA or DJF), matching with the displacement of the Intertropical Convergence Zone (ITCZ) throughout the year [80]. The smallest values (≈0.8 km) are found over land ITCZ. Western China also presents low ABLHs for all seasons. In general, middle latitudes in Northern-Hemisphere regions show shallow ABLHs (<1 km) during the winter season (DJF). MAM and SON periods seem to represent the transitions between DJF and JJA situations, respectively.

All those zones where high ABLHs are found correspond to high-variability regions as shown in Figure 6a, with this relation being more evident over land with a standard deviation of over 1 km in subtropical and tropical regions of South America and Africa, whereas it barely reaches 0.8 km over oceans. In fact, locations where maximum land ABLHs were detected exhibit the greatest seasonal amplitudes. Over these places, ABLH can be 1.5 km higher during (local) wintertime with respect to summertime. Moreover, desert regions like the Sahara, Middle East and Australia show high standard deviation but less pronounced seasonal amplitude, which suggests that ABLH variability here is rather dominated by the intradiurnal ABLH evolution [45]. Variability is weaker over equatorial latitudes, mainly on continents, where the standard deviation is about 0.5 km, and seasonal amplitude is close to 0.0 km. Standard deviation is especially low (around 0.3 km) over the southeastern Pacific and Atlantic Oceans, near the west coasts of South America and Africa. Apart from this, the standard deviation field over oceans is quite homogeneous, exhibiting values between approximately 0.6 and 0.8 km. Also, noteworthy seasonal amplitude is found over North America's littoral and oceanic regions in East Asia, with differences of around −0.8 km.

Analyzing the seasonal behavior, over land, the ABLH seems to manifest an opposing conduct depending on the latitude. The ±30° parallels mark the transition from one behavior zone to another. So, regarding ABLH variability, Earth can be split into three zones: regions between 30°N and 30°S, and regions located at higher latitudes (>30°N and

<30°S). Over intertropical latitudes, ABLH tends to be greater during local wintertime. In other words, in the Northern Hemisphere, the ABLH is higher during the DJF period (except for a region in the Northwest of Africa), whereas in the Southern Hemisphere, the ABLH is larger in the JJA season. During summertime (DJF in the Southern Hemisphere and JJA in the Northern Hemisphere), the ABLH decreases between 0.5 and 1.5 km. The magnitude of change is generally proportional to the winter mean ABLH, that is, the higher ABLH is in winter, the lower it is in summer as shown in Figure 6b. See the case of inland Brazil as a clear example of this behavior: whilst the ABLH remains below 1 km during DJF, it reaches 2.5 km during JJA. However, over middle latitudes (from 30° polewards), ABLH seasonal behavior is inverted. Thus, the ABLH is highest in summer and lowest in winter, though seasonal variations are not as notable as in lower latitudes. For example, in the USA and Europe, ABLH ranges from 0.8–0.9 km in DJF to ≈1.5 km in JJA.

Over oceans, ABLH behavior is similar to that found in low latitudes lands, with higher ABLHs in winter than in summer, although seasonal variations are generally milder than at intertropical continental areas, with standard deviations of around 0.7 km. Nonetheless, two relatively high-variability zones over oceans stand out. In the first zone, the ABLH over the Southern Pacific Ocean changes due to the South Pacific Convergence Zone (SPCZ) seasonal variability. The SPCZ is mostly active between October and April (wet season) where the convection activity is at its maximum so that cloudiness and rainfall are routine [81], leading to low ABLHs (≈1 km) during DJF. In the JJA period, the SPCZ becomes weaker, and its position and extension are not well defined [82], so ABLHs are not much influenced by these phenomena. In the second zone, the Western North Pacific shows a noticeable maximum in DJF, whereas ABLHs are quite shallower in JJA. Such seasonal contrast is attributed to baroclinic systems owing to the difference of temperature between the sea surface and the lower atmosphere, which is larger in DJF [57]. During northern summer, fog is regular in this region [83,84], resulting in low ABLHs. However, during wintertime, ABLHs are relatively high due to cold waves and frontal systems [76].

3.3. ABLH Intradiurnal Fields from Satellite Observations

Figure 7 shows the ABLH mean fields for daytime and nighttime periods, as well as the difference field between them, that is, the diurnal amplitude field. Diurnal variability is clear over land, with higher ABLHs during daytime due to the more convective activity. On average, the ABLH over continents is around 1.3 km during daytime, with Northern Australia being the region where ABLHs are the highest (≈2 km). However, the ABLH barely surpasses 1 km in many areas during nighttime. The diurnal amplitude can even exceed 0.5 km in some regions such as California, the coast of Brazil, the west zone of the Rift Valley, the Middle East, and the whole of Australia. By contrast, tiny variability is observed over the Amazon and Central Africa forests and Indonesia. These areas are located in equatorial latitudes, where ABLHs are typically low and seasonal variations are also weak (Figures 5 and 6). Diurnal variability is practically nonexistent over oceans, where the ABLH exhibits values between approximately 1 and 2 km, depending on the location.

Identifying the ABLH during transition periods can be challenging owing to the appearance of multiple boundaries within the atmospheric profile [85], which directly affects the determination of τ. Furthermore, the paucity of comparable measurements (9 in the best fit; see Table 3) during these intervals might introduce additional bias. Consequently, the τ retrieved for sunrises and sunsets might not be accurate, even if the fit score is high, leading to a mean field of difficult interpretation. For that reason, the ABLH mean field for transition times is not included in this manuscript.

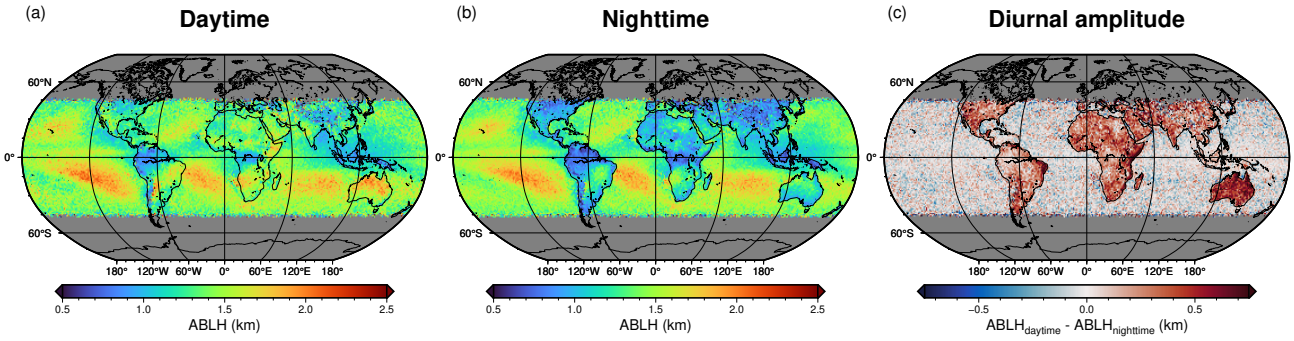

Figure 7. Intradiurnal fields of ABLH above ground level resulting from applying the algorithm derived in Section 3 to refractivity data of COSMIC-2 mission. (**a**,**b**) represent the daytime and nighttime means, respectively. (**c**) depicts the diurnal amplitude, i.e., the difference between daytime and nighttime mean fields ($\text{ABLH}_{\text{daytime}} - \text{ABLH}_{\text{nighttime}}$). Locations in latitudes beyond $\pm 45°$ are out of the COSMIC-2 spatial domain.

3.4. Comparison of the Proposed Algorithm with MRG Method

The fact that refractivity peaks below the MRG are considered implies that the resulting ABLHs are surely lower than those obtained by means of the traditional method (equivalent to using $\tau = 100\%$). Figure 8 shows the differences of seasonal means with respect to the MRG algorithm. As one would expect, tiny differences are observed over oceans since τ here takes a unique value of 99%. Continental regions that exhibit minimum dissimilarities correspond to mountain ranges, specifically, the Himalayas and the Andes, maybe because of the lack of data. Overall, there is not a general pattern over continents, but differences in the fields rather depend on the season. On average, the ABLH difference between both algorithms over land is -0.36 km, with a standard deviation of 0.68 km. In DJF, noticeably greater values are observed in the Northeast of Africa, where ABLH differences do not even reach -0.2 km. On the contrary, large differences (<-0.5 km) are noticed in various near-sea zones: Central America, the Northeast coast of South America, the Western coast of the Asian continent, as well as Indonesia and the Philippines. Similar magnitude differences are also found along a strip in Africa between the equator and the 15°N parallel, approximately. In JJA, the best agreement (differences of about -0.2 km) between algorithms occurs over the middle-east of Brazil and the South of Africa, whereas the greatest differences ($\approx$0.6 km) are located over the West side of the USA, the Amazon basin, the Sahara, the African region between the equator and the 15°S parallel, and the Arabian Peninsula. Note that Africa presents opposed patterns in DJF and JJA, i.e., in those locations where a large ABLH difference is observed in DJF, little difference is found in JJA, and vice versa, which means that the ABLH seasonal amplitude in Africa is lesser with the proposed algorithm. As for the MAM and SON periods, the difference fields are more homogeneous, even though some remarkable differences are observed over the Middle East and the Sahara in MAM, and the Great Rift Valley in SON. It is important to keep in mind that regions where ABLH differences between methods are notable indicate high sensitivity to changes in τ and, therefore, require more detailed and complex analysis, in which further information of atmospheric conditions, like cloud regime, should be taken into consideration.

Concerning intradiurnal differences (Figure 9), the disparate magnitudes obtained for daytime and nighttime are notable. While the difference field for the day phase presents values similar to those retrieved for seasons (≈ -0.35 km), differences in the night phase exceed -0.5 km in many locations over land, even reaching smaller values over vast areas of Western USA, Brazil, Sub-Saharan Africa, the Middle East, and Australia. The greater differences found for nighttime might be caused by the uncertainties related to this period, as well as the τ employed (68%) since its value is more distant to the traditional one (100%) than that used for daytime (82%).

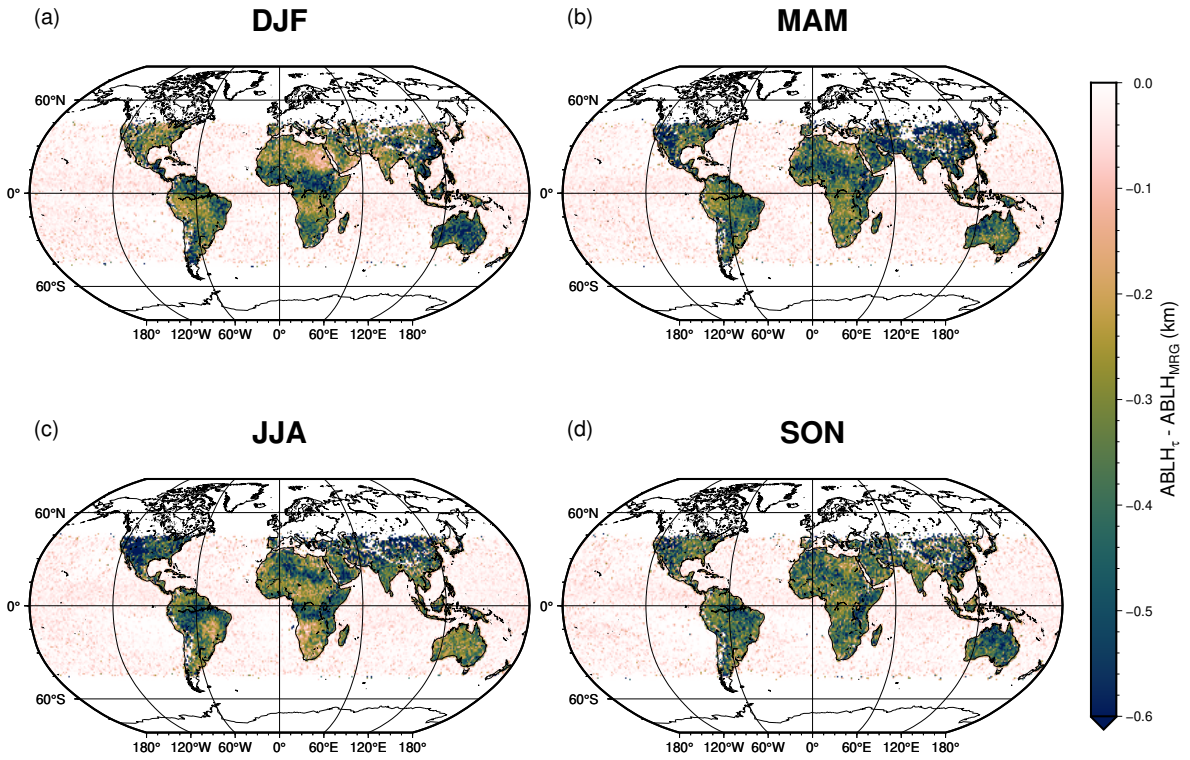

Figure 8. Mean ABLH seasonal differences between the proposed algorithm (using a relative peak strength threshold, $ABLH_\tau$) and the MRG method (equivalent to using $\tau = 100\%$, $ABLH_{MRG}$). Each subpanel refers to one season: (**a**) December, January, and February (DJF); (**b**) March, April, and May (MAM); (**c**) June, July, and August (JJA); (**d**) September, October, and November (SON). Locations in latitudes beyond $\pm 45°$ are out of the COSMIC-2 spatial domain.

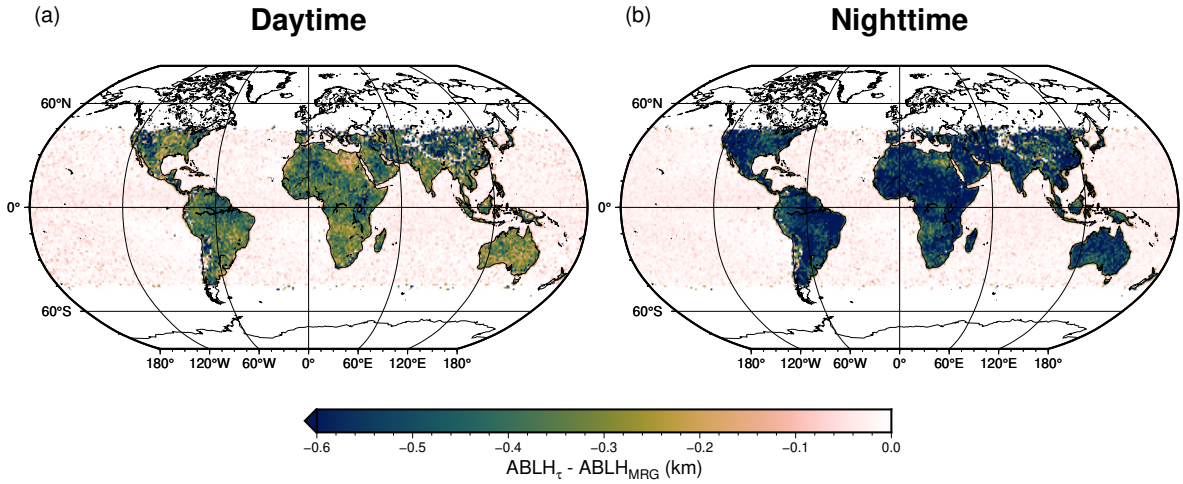

Figure 9. Mean ABLH intradiurnal differences between the proposed algorithm (using a relative peak strength threshold, $ABLH_\tau$) and the MRG method (equivalent to using $\tau = 100\%$, $ABLH_{MRG}$). (**a**) Daytime; (**b**) nighttime. Locations in latitudes beyond $\pm 45°$ are out of the COSMIC-2 spatial domain.

4. Discussion

4.1. ABLH Proposed Algorithm

The validation analysis showed that the best values of τ over land are 82, 68, and 98% for daytime, nighttime, and sunrise/sunset periods, respectively, and 99% for oceanic areas (Table 3). It is noticeable how close the continental daytime τ is to the threshold presented in Santosh [45], who obtained an optimal value equal to 80% for diurnal ABLs.

For the three daily phases considered over land, the best agreement was achieved in comparison with RCS-based methodologies: with lidar data for daytime and nighttime, and with ceilometer data for transition periods. According to the literature, results from these systems are highly reliable during the diurnal phase, especially in the early afternoon, when the peak of maximum convective activity occurs [86] and the CBL covers the full extent of the ABL so that there are no remaining sublayers whose boundaries can deceive the algorithms [87]. Further, agreement can be even better under clear-sky situations [88,89]. On the other hand, doubts about identifying the ABLH during daytime can arise from the presence of elevated aerosol layers [77,90]. Inaccuracy increases at night and in transition periods. According to Geiß et al. [85], the greatest uncertainties usually arise during the transition towards night when new aerosol gradients are prone to appear due to the decay of buoyancy. Moreover, in locations with high emissions of particles, shallow layers tend to emerge. These phenomena lead to the formation of several boundary layers that can cause ambiguities in the ABLH detection algorithm [10]. The high value of τ (98%) retrieved for transition periods could respond to the intention of avoiding those sublayers below the actual ABLH. In the dead of night and early morning, the retrieval of the ABLH may be challenging due to the presence of the SBL, especially if aerosol properties within are similar to those located in the RL.

Comparisons with methodologies that use MWR data did not lead to such good agreement. This could be bound to a series of factors. In general, uncertainties in layer boundary detection are closely related to uncertainties in the atmospheric profiles analyzed, which encompass not only the measured variable but also interpolations and vertical resolution [91]. Refractivity-based methods require knowing three quantities, temperature, pressure, and water vapor pressure, which implies jointly assuming the error associated with each of these variables. Errors can particularly arise from the humidity sensor uncertainties, especially in cold and dry conditions or cloudy situations [28,92]. Concerning temperature-based methods, they present the advantage of only needing information about one variable but are only applicable to instability cases that normally occur during daytime. Moreover, advected air masses containing aerosols whose characteristics differ from local emissions (e.g., long-distance transported desert dust) may alter the temperature profile [93], and thus perturb the thermodynamic method applied [77]. Additionally, another non-negligible source of uncertainty is the number of available observations since a small sample might allow selection bias. The availability of a representative number of measurements may mitigate this effect and faithfully reflect the correct behavior. RCS-based methods, notably those involving lidar systems, are barely prone to suffer from the aforementioned issues. This, together with the high-accuracy lidar technique, makes these instruments very suitable for validation studies.

4.2. ABLH Seasonal Fields

Most of the results concerning the seasonal behavior of ABLH (Figures 5 and 6) are in line with previous studies [4,45,57,76,94], reporting similar extreme values and variability. Nonetheless, some aspects disagree with the literature. The seasonal cycle of ABLH is usually associated with surface heat fluxes, which in turn depend on the amount of incoming solar radiation and ground temperature. Hence, high ABLHs happen during the warm and dry season (normally summer, spring or premonsoon season), whereas low ABLHs occur during the cold and cloudy season (typically winter or monsoon season) [76]. This behavior is not observed over intertropical latitudes in studies that employ GNSS-RO data [45,57,95], including that described in Section 3.2. Given that there are no so-marked seasonal regimes over the tropics and subtropics, it is possible that ABLH variability in these regions might not be dominated by the latitudinal distribution of solar radiation received, but by other factors like ITCZ variability. On regional scales, seasonal variability might be also influenced by local conditions like orography and winds [90,96]. In India, maximum ABLHs are actually reached in MAM (Figure 5b), before the monsoon season.

Maximum ABLHs are commonly connected to convection conditions driven by high ground temperatures, small surface albedo, and low soil humidity [94]. Such circumstances are found over dry subtropical lands, e.g., the Saharan desert. Indeed, over Northern Africa and Australia deserts, daily mean ABLHs exceeding 3 km have been reported [9,30], with the former territory being the region where the highest ABLHs are detected on Earth. Nevertheless, the methodology used in the present study does not reflect this behavior; only summer Eastern Sahara shows prominent ABLHs, whose magnitude does not exceed 2 km.

The ABLH over the ITCZ is a matter of controversy in the literature since ABLH identification can be challenging under strong convection conditions, yielding considerable differences depending on the methodology employed [5,76]. Discrepancies are greater over oceanic ITCZ with special consideration over the Eastern Pacific and Atlantic Oceans. Von Engeln and Teixeira [5] analyzed the ABLH climatology through 20 years of relative humidity data from ECMWF ERA-Interim reanalysis, and found high ABLHs (>1.8 km) over Eastern Pacific ITCZ region for all seasons except MAM which exhibited lower ABL tops. Basha et al. [57] pursued the same objective by applying the wavelet covariance transform [97] to 10 years of refractivity data from several satellite missions, equally observing high ABLHs in ITCZ regions of Eastern Pacific (maximums in DJF season) and Atlantic oceans. The authors of both studies attributed these results to cloud regimes. This behavior perfectly coincides with the retrievals in this research (Figure 5). Over the rest of the ITCZ regions, the mentioned works do not make emphatic conclusions about ABLH climatology. Santosh [45] obtained generalized low values of daily ABLH (<1 km) over the whole ITCZ from COSMIC-2 refractivity data, suggesting a comprehensive decoupling between ABL and clouds. Likewise, McGrath-Spangler and Denning [94] estimated low ABLHs over equatorial latitudes of Pacific and Atlantic oceans from 6 years of lidar backscatter data collected by CALIPSO, only considering non-cloudy situations, associating these results with the upwelling of cold water. Both works contradict the previously cited studies about the magnitude of ABLH over Pacific and Atlantic ITCZ, including this one. Other works focusing on ABLH in marine environments around the ITCZ over the Indian Ocean and Eastern Pacific also reported shallow ABLs with tops below 1 km [98–101]. The results of the present study indicate that ABLHs are rather low over ITCZ regions of the Indian and Eastern Pacific oceans, and South America and Africa continents, concurring with the aforementioned studies. Disagreements between algorithms take place over the Eastern Pacific and Atlantic oceans. The disparity of results comes from the methodology applied. While some methods ascribe the ABLH to the top of clouds, others tend to ignore these boundaries and assign ABLH to a lower level, leading to shallower ABLs. In other words, ABLH uncertainties over this region originate from how the cloud issue is addressed, i.e., whether they are considered to belong to or, otherwise, decoupled from the ABL.

Furthermore, the ITCZ seems to latitudinally expand over Indonesia, Melanesia, and its surroundings, i.e., a large area of low ABLHs in this region, especially in the JJA season, which is addressed in terms of the so-called Double Intertropical Convergence Zone [102,103]. As commented before, the ABLH is sensitive to the seasonal migration of the ITCZ, which moves following the thermal equator (belt around the Earth that exhibits the highest mean temperature for each longitude). Because the Northern Hemisphere is warmer [7,80], the ITCZ shifts more northwards than southwards during the local warm season, and so does the band of low ABLHs over Africa, Asia, and the Indian Ocean, where this phenomenon is clearer [80].

According to Kotthaus et al. [76], ABLH climatology over coasts and littorals is a mixture of land and ocean ABLH characteristics. Moreover, local meteorology, topography, and soil type can influence the ABLH seasonal cycle [96]. Western littorals of Africa and America tend to present shallow ABLs in comparison to the Eastern side, a phenomenon that intensifies in the second half of the year, and it is attributed to strong subsidence and the upwelling of relatively cold water [45]. The ABLH increases offshore due to changes in the cloud regime [104]. In addition, low ABLHs in North American littorals during JJA are

driven by breeze regimes as reported in some studies along the East Coast of the United States [105,106].

4.3. ABLH Intradiurnal Fields

The ABLH intradiurnal fields (Figure 7) agree with those obtained in other studies like that of von Engeln and Teixeira [5], in which ABLH patterns were retrieved at different times using reanalysis data. Nevertheless, just like in the seasonal case, discrepancies occur in Australian and African deserts, where ABLHs greater than 3 km have been estimated for the daytime phase, which differ from the magnitudes obtained in this research.

5. Conclusions

In this work, an improved algorithm to estimate the ABLH from COSMIC-2 refractivity data is presented. The validation procedure involved several methodologies and data sources and consisted of finding the optimal value (τ) of the relative (to MRG) minimum magnitude for a refractivity gradient negative peak to be considered a candidate for representing the ABLH. The best agreement occurs when comparing with RCS-based methods, meaning that lidars and ceilometers are the most suitable instruments for this type of analysis. Over land, the proposed algorithm distinguishes, through the τ parameter, among three periods within the day: daytime, nighttime, and transitions (sunrise and sunset). The corresponding τ's values are 82, 68 and 98%, respectively. One additional τ equaling 99% is used for oceanic zones.

The seasonal mean fields are computed using this algorithm to assess the spatial distribution and variability of ABLH. The resulting patterns are generally modulated by latitude and the underlying surface, as well as cloudiness. The highest values are found over continental areas between 5°S and 20°S of Africa and South America, where ABLH can exceed 2.5 km. These regions, along with desert zones, also exhibit great variability with standard deviations surpassing 1 km. The lowest ABLHs (<1 km) are located over equatorial lands, with the exact position dependent on the season. Moreover, equatorial lands manifest very low variability, showing seasonal amplitudes near 0.0 km and standard deviations of about 0.5 km.

The seasonal behavior of ABLH over continental intertropical latitudes is different from that in middle latitudes. Between 30°N and 30°S, approximately, ABLH is larger during local wintertime. However, the seasonal variability is reversed over higher latitudes; ABLH is greater during local summertime. Over oceans, seasonality is similar to that observed over low latitudes, but it is generally weaker in comparison to land.

Despite the advances made by this and other recent works, in the study of ABLH through satellite observations, more research is needed to further enhance the understanding of the ABL dynamics. In line with this, future studies shall extend the databases since a greater number of observations could lead to the development of better-tuned algorithms. Special focus should be brought into those regions where uncertainty is high, e.g., Eastern Pacific ITCZ. Moreover, progress in measurement technologies and computational codes, as well as the possible implementation of machine learning models, are expected to improve ABL monitoring.

Author Contributions: Conceptualization, G.G.-M., M.J.C. and J.L.G.-R.; methodology, G.G.-M., M.J.C. and J.L.G.-R.; software, G.G.-M.; validation, G.G.-M., M.J.C. and J.L.G.-R.; formal analysis, G.G.-M.; investigation, G.G.-M., M.J.C. and J.L.G.-R.; resources, L.A.-A., J.L.G.-R., M.J.C. and D.B.; data curation, J.A.B.-A., M.J.G.-M., V.S., J.A.-G., S.F.-C.; J.A.-M., A.V., F.N.-G., I.F.-M. and D.B.; writing—original draft preparation, G.G.-M., M.J.C. and J.L.G.-R.; writing—review and editing, all authors; visualization, G.G.-M., M.J.C. and J.L.G.-R.; supervision, M.J.C. and J.L.G.-R.; project administration, M.J.C. and J.L.G.-R.; funding acquisition, L.A.-A., J.L.G.-R., M.J.C. and D.B. All authors have read and agreed to the published version of the manuscript.

Funding: This work was supported by the project PID2020-117825GB-C21 and PID2020-117825GB-C22 funded by MCIN/AEI/10.13039/501100011033. Authors also acknowledge the project P20_00016

C-EXP-366-UGR23 funded by the Government of Andalusia and the European Union through the European Regional Development Fund (ERDF) and the Cost Action PROBE (CA18235).

Data Availability Statement: COSMIC-2 data files are publicly available at the CDAAC (https://cdaac-www.cosmic.ucar.edu/, last access: 15 March 2024). The data used in this study are generated by the Aerosol, Clouds and Trace Gases Research Infrastructure (ACTRIS) and are available from the ACTRIS Data Centre using the following link: https://cloudnet.fmi.fi/file/b608fb9a-af1a-453c-8f6a-23e4b976a38a, last access: 15 March 2024. The MWR and ceilometer data used in this study are generated by the Aerosol, Clouds and Trace Gases Research Infrastructure (ACTRIS) and are available from the ACTRIS Data Centre using the following link: https://cloudnet.fmi.fi, last access: 15 March 2024. EARLINET lidar files are available from the EARLINET Data Portal (https://data.earlinet.org/, last access: 15 March 2024). The accessibility of these files is limited based on the EARLINET criteria. Atmospheric Radiation Measurement (ARM) user facility. Balloon-Borne Sounding System (SONDEWNPN). 30 September 2019 to 1 April 2023 and 31 March 2023 to 13 September 2023, Eastern North Atlantic (ENA) Graciosa Island, Azores, Portugal (C1). Data set accessed 14 July 2023 and 24 November 2023. 18 January 2023 to 28 June 2023, ARM Mobile Facility (EPC) La Jolla, CA; AMF1 (main site for EPCAPE on Scripps Pier) (M1). Data set accessed 28 November 2023. Compiled by E. Keeler, K. Burk and J. Kyrouac. ARM Data Center (http://dx.doi.org/10.5439/1595321, last access: 16 April 2024).

Acknowledgments: We acknowledge ACTRIS and Finnish Meteorological Institute for providing the MWR and ceilometer data set which is available for download from https://cloudnet.fmi.fi (last access: 15 March 2024). Radiosounding data were obtained from the Atmospheric Radiation Measurement (ARM) Program sponsored by the U.S. Department of Energy, Office of Science, Office of Biological and Environmental Research, Climate and Environmental Sciences Division. The authors express their gratitude to Andrew S. Kowalski from the University of Granada for revising the English spelling in this manuscript.

Conflicts of Interest: The authors declare no conflicts of interest.

Abbreviations

The following abbreviations are used in this manuscript:

ABL	Atmospheric Boundary Layer
ABLH	Atmospheric Boundary Layer Height
ACTRIS	Aerosol, Cloud and Trace Gases Research Infrastructure
AGORA	Andalusian Global ObseRvatory of the Atmosphere
ALADIN	Atmospheric Laser Doppler Instrument
ARM	Atmospheric Radiation Measurement
CALIPSO	Cloud-Aerosol Lidar and Infrared Pathfinder Satellite Observations
CBL	Convective Boundary Layer
CDAAC	COSMIC Data Analysis and Archive Center
COSMIC	Constellation Observing System for Meteorology, Ionosphere and Climate
DJF	December, January and February
EARLINET	Europea Aerosol Research Lidar Network
EaRSLab	Earth Remote Sensing Laboratory
ECMWF	European Centre for Medium-Range Weather Forecasts
ENA	Eastern North Atlantic
EPCAPE	Eastern Pacific Cloud Aerosol Precipitation Experiment
EVASO	EVora Atmospheric Sciences Observatory
FT	Free Troposphere
GF	Goodness of Fit function
GNSS	Global Navigation Satellite System
GPS	Global Positioning System
ICT	Institute of Earth Sciences
IISTA	Andalusian Institute for Earth System Research
ITCZ	Intertropical Convergence Zone
IVM	Ion Velocity Meter

JJA	June, July, and August
JPL	Jet Propulsion Laboratory
LEO	Low Earth Orbit
LSG	Lowest Significant Gradient
MAM	March, April, and May
MRG	Minimum Refractivity Gradient
MWR	Microwave Radiometer
NOAA	National Oceanic and Atmospheric Administration
NSPO	National Space Organization
PAOLI	Portable Aerosol and Cloud Lidar
PBL	Planetary Boundary Layer
PM	Parcel Method
RCS	Range-Corrected Signal
RL	Residual Layer
RO	Radio Occultation
SBL	Stable Boundary Layer
SON	September, October, and November
SPALINET	Spanish and Portuguese Aerosol Lidar Network
SPCZ	South Pacific Convergence Zone
TGRS	TriG (GPS, GALILEO and GLONASS) GNSS Radio Occultation System
UCAR	University Corporation for Atmospheric Research

References

1. Seibert, P.; Beyrich, F.; Gryning, S.; Joffre, S.; Rasmussen, A.; Tercier, P. Mixing layer depth determination for dispersion modelling. European Commission. In *COST Action*; European Commission: Brussels, Belgium, 1998.
2. Stull, R.B. *An Introduction to Boundary Layer Meteorology*; Springer Science & Business Media: Berlin/Heidelberg, Germany, 1988; Volume 13.
3. AMS. *Glossary of Meteorology*; American Meteorological Society (AMS): Boston, MA, USA, 2000.
4. Medeiros, B.; Hall, A.; Stevens, B. What controls the mean depth of the PBL? *J. Clim.* **2005**, *18*, 3157–3172. [CrossRef]
5. von Engeln, A.; Teixeira, J. A planetary boundary layer height climatology derived from ECMWF reanalysis data. *J. Clim.* **2013**, *26*, 6575–6590. [CrossRef]
6. Chan, K.M.; Wood, R. The seasonal cycle of planetary boundary layer depth determined using COSMIC radio occultation data. *J. Geophys. Res. Atmos.* **2013**, *118*, 12–422. [CrossRef]
7. Liu, S.; Liang, X.Z. Observed diurnal cycle climatology of planetary boundary layer height. *J. Clim.* **2010**, *23*, 5790–5809. [CrossRef]
8. Palmén, E.; Newton, C.W. *Atmospheric Circulation Systems: Their Structure and Physical Interpretation*; Academic Press: Cambridge, MA, USA, 1969.
9. Garratt, J.R. The atmospheric boundary layer. *Earth-Sci. Rev.* **1994**, *37*, 89–134. [CrossRef]
10. Kotthaus, S.; Bravo-Aranda, J.A.; Collaud Coen, M.; Guerrero-Rascado, J.L.; Costa, M.J.; Cimini, D.; O'Connor, E.J.; Hervo, M.; Alados-Arboledas, L.; Jiménez-Portaz, M.; et al. Atmospheric boundary layer height from ground-based remote sensing: A review of capabilities and limitations. *Atmos. Meas. Tech.* **2023**, *16*, 433–479. [CrossRef]
11. Han, S.; Bian, H.; Tie, X.; Xie, Y.; Sun, M.; Liu, A. Impact of nocturnal planetary boundary layer on urban air pollutants: Measurements from a 250-m tower over Tianjin, China. *J. Hazard. Mater.* **2009**, *162*, 264–269. [CrossRef] [PubMed]
12. Peña, A.; Floors, R.; Sathe, A.; Gryning, S.E.; Wagner, R.; Courtney, M.S.; Larsén, X.G.; Hahmann, A.N.; Hasager, C.B. Ten years of boundary-layer and wind-power meteorology at Høvsøre, Denmark. *Bound.-Layer Meteorol.* **2016**, *158*, 1–26. [CrossRef]
13. Illingworth, A.J.; Cimini, D.; Haefele, A.; Haeffelin, M.; Hervo, M.; Kotthaus, S.; Löhnert, U.; Martinet, P.; Mattis, I.; O'connor, E.; et al. How can existing ground-based profiling instruments improve European weather forecasts? *Bull. Am. Meteorol. Soc.* **2019**, *100*, 605–619. [CrossRef]
14. Barlow, J.; Best, M.; Bohnenstengel, S.I.; Clark, P.; Grimmond, S.; Lean, H.; Christen, A.; Emeis, S.; Haeffelin, M.; Harman, I.N.; et al. Developing a research strategy to better understand, observe, and simulate urban atmospheric processes at kilometer to subkilometer scales. *Bull. Am. Meteorol. Soc.* **2017**, *98*, ES261–ES264. [CrossRef]
15. Vajda, A.; Tuomenvirta, H.; Jokinen, P.; Luomaranta, A.; Makkonen, L.; Tikanmäki, M.; Groenemeijer, P.; Saarikivi, P.; Michaelides, S.; Papadakis, M.; et al. *Probabilities of Adverse Weather Affecting Transport in Europe: Climatology and Scenarios up to the 2050s*; Ilmatieteen Laitos: Helsinki, Finland, 2011.
16. Seibert, P.; Beyrich, F.; Gryning, S.E.; Joffre, S.; Rasmussen, A.; Tercier, P. Review and intercomparison of operational methods for the determination of the mixing height. *Atmos. Environ.* **2000**, *34*, 1001–1027. [CrossRef]
17. Wilczak, J.M.; Cancillo, M.L.; King, C.W. A wind profiler climatology of boundary layer structure above the boreal forest. *J. Geophys. Res. Atmos.* **1997**, *102*, 29083–29100. [CrossRef]

18. Emeis, S.; Schafer, K.; Munkel, C. Surface-based remote sensing of the mixing-layer height-a review. *Meteorol. Z.* **2008**, *17*, 621. [CrossRef] [PubMed]
19. Cimini, D.; Haeffelin, M.; Kotthaus, S.; Löhnert, U.; Martinet, P.; O'Connor, E.; Walden, C.; Coen, M.C.; Preissler, J. Towards the profiling of the atmospheric boundary layer at European scale—introducing the COST Action PROBE. *Bull. Atmos. Sci. Technol.* **2020**, *1*, 23–42. [CrossRef]
20. Collaud Coen, M.; Praz, C.; Haefele, A.; Ruffieux, D.; Kaufmann, P.; Calpini, B. Determination and climatology of the planetary boundary layer height above the Swiss plateau by in situ and remote sensing measurements as well as by the COSMO-2 model. *Atmos. Chem. Phys.* **2014**, *14*, 13205–13221. [CrossRef]
21. Duncan, J.B., Jr.; Bianco, L.; Adler, B.; Bell, T.; Djalalova, I.V.; Riihimaki, L.; Sedlar, J.; Smith, E.N.; Turner, D.D.; Wagner, T.J.; et al. Evaluating convective planetary boundary layer height estimations resolved by both active and passive remote sensing instruments during the CHEESEHEAD19 field campaign. *Atmos. Meas. Tech.* **2022**, *15*, 2479–2502. [CrossRef]
22. Jordan, N.S.; Hoff, R.M.; Bacmeister, J.T. Validation of Goddard Earth Observing System-version 5 MERRA planetary boundary layer heights using CALIPSO. *J. Geophys. Res. Atmos.* **2010**, *115*. [CrossRef]
23. Zhang, W.; Guo, J.; Miao, Y.; Liu, H.; Zhang, Y.; Li, Z.; Zhai, P. Planetary boundary layer height from CALIOP compared to radiosonde over China. *Atmos. Chem. Phys.* **2016**, *16*, 9951–9963. [CrossRef]
24. Flamant, P.; Cuesta, J.; Denneulin, M.L.; Dabas, A.; Huber, D. ADM-Aeolus retrieval algorithms for aerosol and cloud products. *Tellus Dyn. Meteorol. Oceanogr.* **2008**, *60*, 273–286. [CrossRef]
25. Straume, A.G.; Rennie, M.; Isaksen, L.; de Kloe, J.; Marseille, G.J.; Stoffelen, A.; Flament, T.; Stieglitz, H.; Dabas, A.; Huber, D.; et al. ESA's space-based Doppler wind lidar mission Aeolus–First wind and aerosol product assessment results. *EPJ Web Conf.* **2020**, *237*, 01007. [CrossRef]
26. Abril-Gago, J.; Guerrero-Rascado, J.L.; Costa, M.J.; Bravo-Aranda, J.A.; Sicard, M.; Bermejo-Pantaleón, D.; Bortoli, D.; Granados-Muñoz, M.J.; Rodríguez-Gómez, A.; Muñoz-Porcar, C.; et al. Statistical validation of Aeolus L2A particle backscatter coefficient retrievals over ACTRIS/EARLINET stations on the Iberian Peninsula. *Atmos. Chem. Phys.* **2022**, *22*, 1425–1451. [CrossRef]
27. Abril-Gago, J.; Ortiz-Amezcua, P.; Bermejo-Pantaleón, D.; Andújar-Maqueda, J.; Bravo-Aranda, J.A.; Granados-Muñoz, M.J.; Navas-Guzmán, F.; Alados-Arboledas, L.; Foyo-Moreno, I.; Guerrero-Rascado, J.L. Validation activities of Aeolus wind products on the southeastern Iberian Peninsula. *Atmos. Chem. Phys.* **2023**, *23*, 8453–8471. [CrossRef]
28. Seidel, D.J.; Ao, C.O.; Li, K. Estimating climatological planetary boundary layer heights from radiosonde observations: Comparison of methods and uncertainty analysis. *J. Geophys. Res. Atmos.* **2010**, *115*. [CrossRef]
29. Xie, F.; Wu, D.; Ao, C.; Mannucci, A.; Kursinski, E. Advances and limitations of atmospheric boundary layer observations with GPS occultation over southeast Pacific Ocean. *Atmos. Chem. Phys.* **2012**, *12*, 903–918. [CrossRef]
30. Ao, C.O.; Waliser, D.E.; Chan, S.K.; Li, J.L.; Tian, B.; Xie, F.; Mannucci, A.J. Planetary boundary layer heights from GPS radio occultation refractivity and humidity profiles. *J. Geophys. Res. Atmos.* **2012**, *117*. [CrossRef]
31. Ho, S.p.; Peng, L.; Anthes, R.A.; Kuo, Y.H.; Lin, H.C. Marine boundary layer heights and their longitudinal, diurnal, and interseasonal variability in the southeastern Pacific using COSMIC, CALIOP, and radiosonde data. *J. Clim.* **2015**, *28*, 2856–2872. [CrossRef]
32. Liu, J.; Huang, J.; Chen, B.; Zhou, T.; Yan, H.; Jin, H.; Huang, Z.; Zhang, B. Comparisons of PBL heights derived from CALIPSO and ECMWF reanalysis data over China. *J. Quant. Spectrosc. Radiat. Transf.* **2015**, *153*, 102–112. [CrossRef]
33. Von Engeln, A.; Teixeira, J.; Wickert, J.; Buehler, S.A. Using CHAMP radio occultation data to determine the top altitude of the planetary boundary layer. *Geophys. Res. Lett.* **2005**, *32*. [CrossRef]
34. Basha, G.; Ratnam, M.V. Identification of atmospheric boundary layer height over a tropical station using high-resolution radiosonde refractivity profiles: Comparison with GPS radio occultation measurements. *J. Geophys. Res. Atmos.* **2009**, *114*. [CrossRef]
35. Fishbach, F. A satellite method for temperature and pressure below 24 km. *Bull. Am. Meteorol. Soc* **1965**, *9*, 1. [CrossRef]
36. Lusignan, B.; Modrell, G.; Morrison, A.; Pomalaza, J.; Ungar, S. Sensing the Earth's atmosphere with occultation satellites. *Proc. IEEE* **1969**, *57*, 458–467. [CrossRef]
37. Ware, R.; Exner, M.; Feng, D.; Gorbunov, M.; Hardy, K.; Herman, B.; Kuo, Y.; Meehan, T.; Melbourne, W.; Rocken, C.; et al. GPS sounding of the atmosphere from low Earth orbit: Preliminary results. *Bull. Am. Meteorol. Soc.* **1996**, *77*, 19–40. [CrossRef]
38. Kursinski, E.; Hajj, G.; Bertiger, W.; Leroy, S.; Meehan, T.; Romans, L.; Schofield, J.; McCleese, D.; Melbourne, W.; Thornton, C.; et al. Initial results of radio occultation observations of Earth's atmosphere using the Global Positioning System. *Science* **1996**, *271*, 1107–1110. [CrossRef]
39. Kursinski, E.; Hajj, G.; Schofield, J.; Linfield, R.; Hardy, K.R. Observing Earth's atmosphere with radio occultation measurements using the Global Positioning System. *J. Geophys. Res. Atmos.* **1997**, *102*, 23429–23465. [CrossRef]
40. Rocken, C.; Anthes, R.; Exner, M.; Hunt, D.; Sokolovskiy, S.; Ware, R.; Gorbunov, M.; Schreiner, W.; Feng, D.; Herman, B.; et al. Analysis and validation of GPS/MET data in the neutral atmosphere. *J. Geophys. Res. Atmos.* **1997**, *102*, 29849–29866. [CrossRef]
41. Fong, C.J.; Wu, B.H.; Yen, N.; Chen, P. Application of FORMOSAT-3/COSMIC mission to global Earth monitoring. In Proceedings of the Space 2005, Long Beach, CA, USA, 30 August–1 September 2005; p. 6774.
42. Hsu, C.T.; Matsuo, T.; Liu, J.Y. Impact of assimilating the FORMOSAT-3/COSMIC and FORMOSAT-7/COSMIC-2 RO data on the Midlatitude and low-latitude ionospheric specification. *Earth Space Sci.* **2018**, *5*, 875–890. [CrossRef]

43. Ho, S.p.; Anthes, R.A.; Ao, C.O.; Healy, S.; Horanyi, A.; Hunt, D.; Mannucci, A.J.; Pedatella, N.; Randel, W.J.; Simmons, A.; et al. The COSMIC/FORMOSAT-3 radio occultation mission after 12 years: Accomplishments, remaining challenges, and potential impacts of COSMIC-2. *Bull. Am. Meteorol. Soc.* **2020**, *101*, E1107–E1136. [CrossRef]
44. Schreiner, W.S.; Weiss, J.; Anthes, R.A.; Braun, J.; Chu, V.; Fong, J.; Hunt, D.; Kuo, Y.H.; Meehan, T.; Serafino, W.; et al. COSMIC-2 radio occultation constellation: First results. *Geophys. Res. Lett.* **2020**, *47*, e2019GL086841. [CrossRef]
45. Santosh, M. Estimation of daytime planetary boundary layer height (PBLH) over the tropics and subtropics using COSMIC-2/FORMOSAT-7 GNSS–RO measurements. *Atmos. Res.* **2022**, *279*, 106361. [CrossRef]
46. Qiu, C.; Wang, X.; Li, H.; Zhou, K.; Zhang, J.; Li, Z.; Liu, D.; Yuan, H. A Comparison of Atmospheric Boundary Layer Height Determination Methods Using GNSS Radio Occultation Data. *Atmosphere* **2023**, *14*, 1654. [CrossRef]
47. Sokolovskiy, S.; Rocken, C.; Lenschow, D.; Kuo, Y.H.; Anthes, R.; Schreiner, W.; Hunt, D. Observing the moist troposphere with radio occultation signals from COSMIC. *Geophys. Res. Lett.* **2007**, *34*. [CrossRef]
48. Guo, P.; Kuo, Y.H.; Sokolovskiy, S.; Lenschow, D. Estimating atmospheric boundary layer depth using COSMIC radio occultation data. *J. Atmos. Sci.* **2011**, *68*, 1703–1713. [CrossRef]
49. Tien, J.Y.; Okihiro, B.B.; Esterhuizen, S.X.; Franklin, G.W.; Meehan, T.K.; Munson, T.N.; Robison, D.E.; Turbiner, D.; Young, L.E. Next generation scalable spaceborne GNSS science receiver. In Proceedings of the 2012 international technical meeting of the institute of navigation, Newport Beach, CA, USA, 30 January–1 February 2012; pp. 882–914.
50. Esterhuizen, S.; Franklin, G.; Hurst, K.; Mannucci, A.; Meehan, T.; Webb, F.; Young, L. TriG-A GNSS precise orbit and radio occultation space receiver. In Proceedings of the 22nd International Technical Meeting of the Satellite Division of The Institute of Navigation (ION GNSS 2009), Savannah, GA, USA, 22–25 September 2009; pp. 1442–1446.
51. Ho, S.P.; Zhou, X.; Shao, X.; Zhang, B.; Adhikari, L.; Kireev, S.; He, Y.; Yoe, J.G.; Xia-Serafino, W.; Lynch, E. Initial assessment of the COSMIC-2/FORMOSAT-7 neutral atmosphere data quality in NESDIS/STAR using in situ and satellite data. *Remote. Sens.* **2020**, *12*, 4099. [CrossRef]
52. Kuo, Y.H.; Wee, T.K.; Sokolovskiy, S.; Rocken, C.; Schreiner, W.; Hunt, D.; Anthes, R. Inversion and error estimation of GPS radio occultation data. *J. Meteorol. Soc. Jpn. Ser.* **2004**, *82*, 507–531. [CrossRef]
53. Ho, S.p.; Kirchengast, G.; Leroy, S.; Wickert, J.; Mannucci, A.J.; Steiner, A.; Hunt, D.; Schreiner, W.; Sokolovskiy, S.; Ao, C.; et al. Estimating the uncertainty of using GPS radio occultation data for climate monitoring: Intercomparison of CHAMP refractivity climate records from 2002 to 2006 from different data centers. *J. Geophys. Res. Atmos.* **2009**, *114*. [CrossRef]
54. Ho, S.p.; Hunt, D.; Steiner, A.K.; Mannucci, A.J.; Kirchengast, G.; Gleisner, H.; Heise, S.; von Engeln, A.; Marquardt, C.; Sokolovskiy, S.; et al. Reproducibility of GPS radio occultation data for climate monitoring: Profile-to-profile inter-comparison of CHAMP climate records 2002 to 2008 from six data centers. *J. Geophys. Res. Atmos.* **2012**, *117*. [CrossRef]
55. Wee, T.K. A variational regularization of Abel transform for GPS radio occultation. *Atmos. Meas. Tech.* **2018**, *11*, 1947–1969. [CrossRef]
56. Straume, A.; Schuettemeyer, D.; Von Bismarck, J.; Kanitz, T.; Fehr, T. *Aeolus Scientific Calibration and Validation Implementation Plan*; European Space Research and Technology Centre: Noordwijk, The Netherlands, 2019.
57. Basha, G.; Kishore, P.; Ratnam, M.V.; Ravindra Babu, S.; Velicogna, I.; Jiang, J.H.; Ao, C.O. Global climatology of planetary boundary layer top obtained from multi-satellite GPS RO observations. *Clim. Dyn.* **2019**, *52*, 2385–2398. [CrossRef]
58. Rose, T.; Crewell, S.; Löhnert, U.; Simmer, C. A network suitable microwave radiometer for operational monitoring of the cloudy atmosphere. *Atmos. Res.* **2005**, *75*, 183–200. [CrossRef]
59. Vaquero-Martínez, J.; Antón, M.; Costa, M.J.; Bortoli, D.; Navas-Guzmán, F.; Alados-Arboledas, L. Microwave radiometer, sun-photometer and GNSS multi-comparison of integrated water vapor in Southwestern Europe. *Atmos. Res.* **2023**, *287*, 106698. [CrossRef]
60. Heese, B.; Flentje, H.; Althausen, D.; Ansmann, A.; Frey, S. Ceilometer lidar comparison: Backscatter coefficient retrieval and signal-to-noise ratio determination. *Atmos. Meas. Tech.* **2010**, *3*, 1763–1770. [CrossRef]
61. Cazorla, A.; Casquero-Vera, J.A.; Román, R.; Guerrero-Rascado, J.L.; Toledano, C.; Cachorro, V.E.; Orza, J.A.G.; Cancillo, M.L.; Serrano, A.; Titos, G.; et al. Near-real-time processing of a ceilometer network assisted with sun-photometer data: Monitoring a dust outbreak over the Iberian Peninsula. *Atmos. Chem. Phys.* **2017**, *17*, 11861–11876. [CrossRef]
62. Althausen, D.; Engelmann, R.; Baars, H.; Heese, B.; Ansmann, A.; Müller, D.; Komppula, M. Portable Raman lidar PollyXT for automated profiling of aerosol backscatter, extinction, and depolarization. *J. Atmos. Ocean. Technol.* **2009**, *26*, 2366–2378. [CrossRef]
63. Salgueiro, V.; Costa, M.J.; Guerrero-Rascado, J.L.; Couto, F.T.; Bortoli, D. Characterization of forest fire and Saharan desert dust aerosols over south-western Europe using a multi-wavelength Raman lidar and Sun-photometer. *Atmos. Environ.* **2021**, *252*, 118346. [CrossRef]
64. Preißler, J.; Wagner, F.; Pereira, S.; Guerrero-Rascado, J. Multi-instrumental observation of an exceptionally strong Saharan dust outbreak over Portugal. *J. Geophys. Res. Atmos.* **2011**, *116*. [CrossRef]
65. Pappalardo, G.; Amodeo, A.; Apituley, A.; Comeron, A.; Freudenthaler, V.; Linné, H.; Ansmann, A.; Bösenberg, J.; D'Amico, G.; Mattis, I.; et al. EARLINET: Towards an advanced sustainable European aerosol lidar network. *Atmos. Meas. Tech.* **2014**, *7*, 2389–2409. [CrossRef]

66. Sicard, M.; Molero, F.; Guerrero-Rascado, J.L.; Pedrós, R.; Expósito, F.J.; Córdoba-Jabonero, C.; Bolarín, J.M.; Comerón, A.; Rocadenbosch, F.; Pujadas, M.; et al. Aerosol LiDAR intercomparison in the framework of SPALINET—The Spanish LiDAR network: Methodology and results. *IEEE Trans. Geosci. Remote. Sens.* **2009**, *47*, 3547–3559. [CrossRef]
67. Holdridge, D. *Balloon-Borne Sounding System (SONDE) Instrument Handbook*; Technical Report, DOE Office of Science Atmospheric Radiation Measurement (ARM) Program; U.S. Department of Energy, Office of Science, Office of Biological and Environmental Research: Washington, DC, USA, 2020.
68. Quarteroni, A.; Sacco, R.; Saleri, F. *Numerical Mathematics*; Springer Science & Business Media: Berlin/Heidelberg, Germany, 2006; Volume 37.
69. Cartwright, K.V. Simpson's rule cumulative integration with MS Excel and irregularly-spaced data. *J. Math. Sci. Math. Educ.* **2017**, *12*, 1–9.
70. List, R.J. *Smithsonian Meteorological Tables*; Smithsonian miscellaneous collections; NWS Weather Forecast Offices: Silver Spring, MD, USA, 1951.
71. Savitzky, A.; Golay, M.J. Smoothing and differentiation of data by simplified least squares procedures. *Anal. Chem.* **1964**, *36*, 1627–1639. [CrossRef]
72. de Arruda Moreira, G.; Guerrero-Rascado, J.L.; Bravo-Aranda, J.A.; Foyo-Moreno, I.; Cazorla, A.; Alados, I.; Lyamani, H.; Landulfo, E.; Alados-Arboledas, L. Study of the planetary boundary layer height in an urban environment using a combination of microwave radiometer and ceilometer. *Atmos. Res.* **2020**, *240*, 104932. [CrossRef]
73. Stull, R.B. *Meteorology for Scientists and Engineers: A Technical Companion Book with Ahrens' Meteorology Today*; Brooks/Cole: Salt Lake City, UL, USA, 2000.
74. Holzworth, G.C. Estimates of mean maximum mixing depths in the contiguous United States. *Mon. Weather. Rev.* **1964**, *92*, 235–242. [CrossRef]
75. Menut, L.; Flamant, C.; Pelon, J.; Flamant, P.H. Urban boundary-layer height determination from lidar measurements over the Paris area. *Appl. Opt.* **1999**, *38*, 945–954. [CrossRef]
76. Kotthaus, S.; Bravo-Aranda, J.; Collaud Coen, M.; Guerrero-Rascado, J.; Costa, M.J.; Cimini, D.; O'Connor, E.; Maxime, H.; Arboledas, L.; Jiménez-Portaz, M.; et al. Atmospheric boundary layer height from ground-based remote sensing: A review of capabilities and limitations. *Atmos. Meas. Tech. Discuss.* 2022, *2022*, 1–88. [CrossRef]
77. Granados-Muñoz, M.; Navas-Guzmán, F.; Bravo-Aranda, J.; Guerrero-Rascado, J.; Lyamani, H.; Fernández-Gálvez, J.; Alados-Arboledas, L. Automatic determination of the planetary boundary layer height using lidar: One-year analysis over southeastern Spain. *J. Geophys. Res. Atmos.* **2012**, *117*. [CrossRef]
78. Renju, R.; Raju, C.S.; Mishra, M.; Mathew, N.; Rajeev, K.; Moorthy, K.K. Atmospheric boundary layer characterization using multiyear ground-based microwave radiometric observations over a tropical coastal station. *IEEE Trans. Geosci. Remote. Sens.* **2017**, *55*, 6877–6882. [CrossRef]
79. Carpenter, T. Thermal Properties of Dry and Saturated Soils. Master's Thesis, University of Tennessee, Knoxville, TN, USA, 2019.
80. Schneider, T.; Bischoff, T.; Haug, G.H. Migrations and dynamics of the intertropical convergence zone. *Nature* **2014**, *513*, 45–53. [CrossRef] [PubMed]
81. Haffke, C.; Magnusdottir, G. The South Pacific Convergence Zone in three decades of satellite images. *J. Geophys. Res. Atmos.* **2013**, *118*, 10–839. [CrossRef]
82. Vincent, D.G. The South Pacific convergence zone (SPCZ): A review. *Mon. Weather. Rev.* **1994**, *122*, 1949–1970. [CrossRef]
83. Klein, S.A.; Hartmann, D.L. The seasonal cycle of low stratiform clouds. *J. Clim.* **1993**, *6*, 1587–1606. [CrossRef]
84. Teixeira, J. Simulation of fog with the ECMWF prognostic cloud scheme. *Q. J. R. Meteorol. Soc.* **1999**, *125*, 529–552. [CrossRef]
85. Geiß, A.; Wiegner, M.; Bonn, B.; Schäfer, K.; Forkel, R.; von Schneidemesser, E.; Münkel, C.; Chan, K.L.; Nothard, R. Mixing layer height as an indicator for urban air quality? *Atmos. Meas. Tech.* **2017**, *10*, 2969–2988. [CrossRef]
86. Milroy, C.; Martucci, G.; Lolli, S.; Loaec, S.; Sauvage, L.; Xueref-Remy, I.; Lavrič, J.V.; Ciais, P.; Feist, D.G.; Biavati, G.; et al. An assessment of pseudo-operational ground-based light detection and ranging sensors to determine the boundary-layer structure in the coastal atmosphere. *Adv. Meteorol.* **2012**, *2012*, 929080. [CrossRef]
87. Toledo, D.; Córdoba-Jabonero, C.; Adame, J.A.; De La Morena, B.; Gil-Ojeda, M. Estimation of the atmospheric boundary layer height during different atmospheric conditions: A comparison on reliability of several methods applied to lidar measurements. *Int. J. Remote. Sens.* **2017**, *38*, 3203–3218. [CrossRef]
88. Barlow, J.F.; Dunbar, T.; Nemitz, E.; Wood, C.R.; Gallagher, M.; Davies, F.; O'Connor, E.; Harrison, R. Boundary layer dynamics over London, UK, as observed using Doppler lidar during REPARTEE-II. *Atmos. Chem. Phys.* **2011**, *11*, 2111–2125. [CrossRef]
89. de Arruda Moreira, G.; Guerrero-Rascado, J.L.; Bravo-Aranda, J.A.; Benavent-Oltra, J.A.; Ortiz-Amezcua, P.; Róman, R.; Bedoya-Velásquez, A.E.; Landulfo, E.; Alados-Arboledas, L. Study of the planetary boundary layer by microwave radiometer, elastic lidar and Doppler lidar estimations in Southern Iberian Peninsula. *Atmos. Res.* **2018**, *213*, 185–195. [CrossRef]
90. Tang, G.; Zhang, J.; Zhu, X.; Song, T.; Münkel, C.; Hu, B.; Schäfer, K.; Liu, Z.; Zhang, J.; Wang, L.; et al. Mixing layer height and its implications for air pollution over Beijing, China. *Atmos. Chem. Phys.* **2016**, *16*, 2459–2475. [CrossRef]
91. Seidel, D.J.; Zhang, Y.; Beljaars, A.; Golaz, J.C.; Jacobson, A.R.; Medeiros, B. Climatology of the planetary boundary layer over the continental United States and Europe. *J. Geophys. Res. Atmos.* **2012**, *117*. [CrossRef]
92. Wang, X.; Wang, K. Estimation of atmospheric mixing layer height from radiosonde data. *Atmos. Meas. Tech.* **2014**, *7*, 1701–1709. [CrossRef]

93. Guerrero-Rascado, J.L.; Olmo, F.; Avilés-Rodríguez, I.; Navas-Guzmán, F.; Pérez-Ramírez, D.; Lyamani, H.; Alados Arboledas, L. Extreme Saharan dust event over the southern Iberian Peninsula in september 2007: Active and passive remote sensing from surface and satellite. *Atmos. Chem. Phys.* **2009**, *9*, 8453–8469. [CrossRef]
94. McGrath-Spangler, E.L.; Denning, A.S. Global seasonal variations of midday planetary boundary layer depth from CALIPSO space-borne LIDAR. *J. Geophys. Res. Atmos.* **2013**, *118*, 1226–1233. [CrossRef]
95. Ratnam, M.; Basha, S. A robust method to determine global distribution of atmospheric boundary layer top from COSMIC GPS RO measurements. *Atmos. Sci. Lett.* **2010**, *11*, 216–222. [CrossRef]
96. Bianco, L.; Djalalova, I.; King, C.; Wilczak, J. Diurnal evolution and annual variability of boundary-layer height and its correlation to other meteorological variables in California's Central Valley. *Bound.-Layer Meteorol.* **2011**, *140*, 491–511. [CrossRef]
97. Brooks, I.M. Finding boundary layer top: Application of a wavelet covariance transform to lidar backscatter profiles. *J. Atmos. Ocean. Technol.* **2003**, *20*, 1092–1105. [CrossRef]
98. Manghnani, V.; Raman, S.; Niyogi, D.S.; Parameswara, V.; Morrison, J.M.; Ramana, S.; Raju, J. Marine boundary-layer variability over the Indian Ocean during INDOEX (1998). *Bound.-Layer Meteorol.* **2000**, *97*, 411–430. [CrossRef]
99. Subrahamanyam, D.B.; Ramachandran, R.; Gupta, K.S.; Mandal, T.K. Variability of mixed-layer heights over the Indian Ocean and central Arabian Sea during INDOEX, IFP-99. *Bound.-Layer Meteorol.* **2003**, *107*, 683–695. [CrossRef]
100. Zeng, X.; Brunke, M.A.; Zhou, M.; Fairall, C.; Bond, N.A.; Lenschow, D.H. Marine atmospheric boundary layer height over the eastern Pacific: Data analysis and model evaluation. *J. Clim.* **2004**, *17*, 4159–4170. [CrossRef]
101. Johnson, R.H.; Ciesielski, P.E. Multiscale variability of the atmospheric boundary layer during DYNAMO. *J. Atmos. Sci.* **2017**, *74*, 4003–4021. [CrossRef]
102. Zhang, C. Double ITCZs. *J. Geophys. Res. Atmos.* **2001**, *106*, 11785–11792. [CrossRef]
103. Meenu, S.; Rajeev, K.; Parameswaran, K.; Suresh Raju, C. Characteristics of the double intertropical convergence zone over the tropical Indian Ocean. *J. Geophys. Res. Atmos.* **2007**, *112*. [CrossRef]
104. Wood, R.; Bretherton, C.S. Boundary layer depth, entrainment, and decoupling in the cloud-capped subtropical and tropical marine boundary layer. *J. Clim.* **2004**, *17*, 3576–3588. [CrossRef]
105. Niyogi, D. Urban impacts on regional rainfall climatology. In Proceedings of the Ninth International Conference on Urban Climate/12th Symposium on the Urban Environment, Toulouse, France, IAUC and American Meteorological Society, UCP9-7, Toulouse, France, 20–24 July 2015. Available online: http://www.meteo.fr/icuc9/presentations/UCP/UCP9-7.pdf (accessed on 4 February 2024)
106. Melecio-Vázquez, D.; González-Cruz, J.; Arend, M.; Han, Z.; Gutierrez, E.; Dempsey, M.; Booth, J. New York metro-area boundary layer catalogue: Boundary layer height and stability conditions from long-term observations. In Proceedings of the Ninth International Conference on Urban Climate/12th Symposium on the Urban Environment, Toulouse, France, IAUC and American Meteorological Society, Toulouse, France, 20–24 July 2015.